











Probing Intra-Halo Light with Galaxy Stacking in CIBER Images

YUN-TING CHENG ¹, TOSHIAKI ARAI,² PRIYADARSHINI BANGALE ³, JAMES J. BOCK,^{1,4} TZU-CHING CHANG ^{4,1},
ASANTHA COORAY,⁵ RICHARD M. FEDER ¹, PHILLIP M. KORNGUT,¹ DAE HEE LEE,⁶ LUNJUN LIU,¹
TOSHIO MATSUMOTO ², SHUJI MATSUURA ⁷, CHI H. NGUYEN ³, KEI SANO ⁸, KOHJI TSUMURA ⁹ AND
MICHAEL ZEMCOV ^{3,4}

¹*California Institute of Technology, 1200 E. California Boulevard, Pasadena, CA 91125, USA*

²*Institute of Space and Astronautical Science, Japan Aerospace Exploration Agency, Kanagawa 252-5210, Japan*

³*Center for Detectors, School of Physics and Astronomy, Rochester Institute of Technology, 1 Lomb Memorial Drive, Rochester, New York 14623, USA*

⁴*Jet Propulsion Laboratory, California Institute of Technology, 4800 Oak Grove Drive, Pasadena, CA 91109, USA*

⁵*Department of Physics and Astronomy, University of California, Irvine, CA 92697, U.S.A.*

⁶*Korea Astronomy and Space Science Institute (KASI), Daejeon 305-348, Republic of Korea*

⁷*School of Science and Technology, Kwansei Gakuin University, Sanda, Hyogo 669-1337, Japan*

⁸*Kyushu Institute of Technology, 1-1 Sensui-cho, Tobata, Kitakyushu, Fukuoka 804-8550, Japan*

⁹*Department of Natural Science, Faculty of Science and Engineering, Tokyo City University, Tokyo, 158-8557, Japan*

ABSTRACT

We study the stellar halos of $0.2 \lesssim z \lesssim 0.5$ galaxies with stellar masses spanning $M_* \sim 10^{10.5}$ to $10^{12} M_\odot$ (approximately L_* galaxies at this redshift) using imaging data from the Cosmic Infrared Background Experiment (CIBER). A previous CIBER fluctuation analysis suggested that intra-halo light (IHL) contributes a significant portion of the near-infrared extragalactic background light (EBL), the integrated emission from all sources throughout cosmic history. In this work, we carry out a stacking analysis with a sample of $\sim 30,000$ Sloan Digital Sky Survey (SDSS) photometric galaxies from CIBER images in two near-infrared bands (1.1 and $1.8 \mu\text{m}$) to directly probe the IHL associated with these galaxies. We stack galaxies in five sub-samples split by brightness, and detect an extended galaxy profile, beyond the instrument point spread function (PSF), derived by stacking stars. We jointly fit a model for the inherent galaxy light profile, plus large-scale one- and two-halo clustering to measure the extended galaxy IHL. We detect non-linear one-halo clustering in the $1.8 \mu\text{m}$ band, at a level consistent with numerical simulations. **We study the fraction of galaxy light in the extended region and how it evolves with cosmic time. By extrapolating the fraction we measure to all galaxy masses scales, and applying a Schechter luminosity function, we find $\sim 50\%/30\%$ of the total galaxy light budget is from the outskirts of the galaxies at $r > 10/20$ kpc, respectively. These results are new at near-infrared wavelengths at the L_* mass scale, which are the representative galaxy populations that contain majority of the total integrated galactic light. Our results suggest that the IHL emission and one-halo clustering could have appreciable contributions to the amplitude of large-scale EBL background fluctuations.**

Keywords: cosmology: observations – diffuse radiation — large-scale structure of universe

1. INTRODUCTION

In the standard cosmological paradigm, galaxies grow hierarchically through merger and accretion. Galaxies accreting onto more massive systems become disrupted, and stars stripped away from their parent galaxies be-

come redistributed in the merged dark matter halo. This results in extended stellar halos that are known to span tens or hundreds of kilo-parsecs. The stellar emission from this material is sometimes referred to as “intra-halo light” (IHL), or in massive galaxy clusters as “intra-cluster light” (ICL).

The properties of stellar halos across a wide range of mass scales have been extensively studied using analytical models (e.g., Purcell et al. 2007) and N-body sim-

ulations (e.g., Bullock & Johnston 2005; Conroy et al. 2007; Rudick et al. 2009; Cooper et al. 2010, 2013, 2015; Rodriguez-Gomez et al. 2016; Elias et al. 2018). Several observations have constrained the ICL content in galaxy clusters (e.g., Lin & Mohr 2004; Burke et al. 2015; Gonzalez et al. 2005, 2007, 2005), as well as stellar halos in lower mass systems by deeply imaging individual galaxies (e.g., Tal et al. 2009; Martínez-Delgado et al. 2010; Abraham & van Dokkum 2014; van Dokkum et al. 2014; Huang et al. 2018) or through stacking (e.g., Zibetti et al. 2005; D’Souza et al. 2014; Zhang et al. 2019; Wang et al. 2019).

An independent way to study the aggregate emission from diffuse sources like IHL is through measurements of the extragalactic background light (EBL), which encodes the integrated emission from all sources across cosmic history (Cooray 2016). Absolute optical and near-infrared EBL photometry has proven challenging as measurements must tightly control systematic errors and carefully model and subtract local foregrounds (e.g., Kawara et al. 2017; Zemcov et al. 2017; Matsuura et al. 2017; Matsumoto et al. 2018; Lauer et al. 2020). Several authors (Bernstein 2007; Levenson et al. 2007; Tsumura et al. 2013a; Matsumoto et al. 2015; Sano et al. 2015; Zemcov et al. 2017; Matsuura et al. 2017; Sano et al. 2020; Lauer et al. 2020) have reported potential detections above the integrated galaxy light (IGL) derived from galaxy counts (Keenan et al. 2010; Domínguez et al. 2011; Helgason et al. 2012; Driver et al. 2016; Saldana-Lopez et al. 2020; Koushan et al. 2021), which may indicate the existence of extragalactic emission missed in source counting surveys.

Additionally, EBL fluctuation analyses have also consistently reported excess fluctuations over those expected from the IGL (Kashlinsky et al. 2005; Thompson et al. 2007; Matsumoto et al. 2011; Kashlinsky et al. 2012; Cooray et al. 2012; Zemcov et al. 2014; Mitchell-Wynne et al. 2015; Seo et al. 2015; Kim et al. 2019; Matsumoto & Tsumura 2019). One explanation is emission from the epoch of reionization (Kashlinsky et al. 2005; Matsumoto et al. 2011; Kashlinsky et al. 2012; Mitchell-Wynne et al. 2015), while other studies suggest IHL contributes most of the excess fluctuations (Cooray et al. 2012). In particular, Zemcov et al. (2014) interpret imaging data from the *Cosmic Infrared Background Experiment* (CIBER) as arising from an IHL intensity comparable to the IGL at near-infrared wavelengths. This result would imply that stars diffusely scattered in dark matter halos may account for a non-negligible fraction of the near-IR cosmic radiation budget. **The absorption spectra from blazars constrain the EBL column density along the line of sight** (e.g., Aharonian et al. 2006, 2007;

MAGIC Collaboration et al. 2008; Abdo et al. 2010; Ackermann et al. 2012; H. E. S. S. Collaboration et al. 2017; Ackermann et al. 2018; Abeysekara et al. 2019; Acciari et al. 2019; Abdalla et al. 2020). **While IHL is generally produced at low redshifts, improving the uncertainties in its redshift history helps place IHL in the context of these constraints.**

In this work, we further constrain the IHL using CIBER broad band imaging. Rather than studying EBL intensity fluctuations as in Zemcov et al. (2014), we perform a stacking analysis to directly probe the stellar halos around galaxies. We stack a sample of $\sim 30,000$ Sloan Digital Sky Survey (SDSS) photometric galaxies at $z \sim 0.2 - 0.5$ across five 2×2 deg² fields. Our samples span a range of stellar masses at approximately L_* scales at this redshift (Muzzin et al. 2013). Although we only study stellar halos around a subset of galaxies, rather than the aggregate population as probed by fluctuations, stacking provides a direct path to probe the IHL associated with this sample. Stacking complements fluctuation measurements by probing the relationship between individual galaxies and their stellar halos. Stacking also allows us to investigate how stellar halos depend on host galaxy properties, e.g. stellar mass, redshift, etc. A complementary fluctuation analysis of these same data is currently in progress.

This paper is organized as follows. First, we introduce CIBER in Sec. 2 and the data processing in Sec. 3. Sec. 4 and 5 describe the external data sets used in this work, including observed and simulated source catalogs. Sec. 6 details the stacking procedure, and Sec. 7 describes the point spread function (PSF) model. The stacking results are presented in Sec. 8. Sec. 9 introduces the theoretical model we use to fit the data, and the parameter fitting procedure. The results on model parameter constraints are given in Sec. 10, and further discussion is presented in Sec. 11. Sec. 12 summarizes the paper. Throughout this work, we assume a flat Λ CDM cosmology with $n_s = 0.97$, $\sigma_8 = 0.82$, $\Omega_m = 0.26$, $\Omega_b = 0.049$, $\Omega_\Lambda = 0.69$, and $h = 0.68$, consistent with the measurement from *Planck* (Planck Collaboration et al. 2016). All fluxes are quoted in the AB magnitude system.

2. CIBER EXPERIMENT

CIBER¹ (Zemcov et al. 2013) is a rocket-borne instrument designed to characterize the near-infrared EBL. CIBER consists of four instruments: two wide-field imagers (Bock et al. 2013), a narrow-band spectrometer (Korngut et al. 2013), and a low-resolution spectrom-

¹ <https://ciberrocket.github.io/>

Table 1. CIBER Observing Fields

Field Name	R.A. (°)	Dec. (°)	Time After Launch (sec)	Number of Frames Used	Integration Time (sec)
Elat10	191.50	8.25	387-436	24	42.72
Elat30	193.94	28.00	450-500	9	16.02
BootesB	218.11	33.18	513-569	29	51.62
BootesA	219.25	34.83	581-636	28	49.84
SWIRE(ELAIS-N1)	241.53	54.77	655-705	25	44.50

NOTE—We discard the beginning part of Elat30 field integration due to pointing instability.

154 eter (Tsumura et al. 2013b). CIBER has flown four
 155 times in February 2009, July 2010, March 2012, and
 156 June 2013. The first three CIBER flights were launched
 157 at White Sands Missile Range, New Mexico on a Terrier-
 158 Black Brant IX rocket. These flights reached ~ 330 km
 159 apogee with ~ 240 sec of exposure time, and the pay-
 160 load was recovered for future flights. The fourth flight
 161 was a non-recovery flight launched 3:05 UTC 2013 June
 162 6 from Wallops Flight Facility, Virginia on a four-stage
 163 Black Brant XII rocket. The payload reached 550 km
 164 altitude, much higher than the two-stage rocket used in
 165 the previous three flights. This gives more exposure time
 166 (335 sec) for observing more science fields with long in-
 167 tegrations to achieve better sensitivity and systematics
 168 control.

169 This work presents the first science results from the
 170 CIBER fourth flight imager data. The data from previ-
 171 ous flights have been studied with a fluctuation analysis,
 172 published in Zemcov et al. (2014). With a large field
 173 of view and low sky background above the atmosphere,
 174 CIBER imaging provides fidelity on angular scales from
 175 $7''$ to 2° . For stacking, CIBER imaging can trace low
 176 surface brightness emission on degree angular scales pro-
 177 viding a unique dataset compared with ground-based or
 178 small field-of-view space-borne studies. Each CIBER
 179 imager uses a 1024×1024 pixel HAWAII-1 HgCdTe de-
 180 tector. The two imagers are identical except for their
 181 $\lambda/\Delta\lambda \sim 2$ filters, which are centered at 1.05 and 1.79
 182 μm^2 .

183 During its fourth flight, CIBER observed eight sci-
 184 ence fields with ~ 50 sec integrations sampled at 1.78
 185 sec intervals. We discard the first three fields in this
 186 analysis due to contamination from airglow that pro-
 187 duces a strong non-uniform emission across the images
 188 that requires aggressive filtering which also significantly

189 reduces our signal (Zemcov et al. 2014). Table 1 sum-
 190 marizes the sky coordinates and the integration time of
 191 the five science fields used in this work. In the begin-
 192 ning of the Elat30 integration, the rocket’s pointing was
 193 not stable which has the effect of smearing the PSF on
 194 the sky. As a result, we only use the last 16 sec of this
 195 integration in our analysis.

3. DATA PROCESSING

197 In this section, we describe the data reduction from
 198 the raw flight data to the final images used for stacking.

3.1. Raw Time Stream to Images

199 The raw imager data provides a time series for each
 200 pixel. We fit a slope to the time stream to obtain the
 201 photocurrent in each pixel, and convert the values from
 202 the raw analog-to-digital units (ADU) to $e^- \text{ s}^{-1}$ using
 203 known array gain factors.

204 The HAWAII-1 detector is linearly responsive to in-
 205 coming flux over a certain dynamic range. For pixels
 206 pointing at bright sources, the detectors saturate and
 207 have a non-linear flux dependence, even for short inte-
 208 grations (Bock et al. 2013). In any pixel that collects
 209 more than 5,000 ADU over the full integration only the
 210 first four frames are used in the photocurrent estimate.
 211 Hereafter, the term “raw image” refers to the photocur-
 212 rent map after this linearity correction. Panel A of Fig. 1
 213 and Fig. 2 show the raw images of the SWIRE field in
 214 the CIBER 1.1 and 1.8 μm bands, respectively.
 215

3.2. Dark Current

216 In the absence of incoming photons, the detectors have
 217 a nonzero response, commonly referred to as “dark cur-
 218 rent”, due to thermally produced charge carriers and
 219 multiplexer glow. The detector dark current is mea-
 220 sured before each flight with the telescopes’ cold shut-
 221 ters closed. We obtain a dark current template for each
 222 detector by averaging 11 dark images and then subtract-
 223 ing each template from the corresponding raw images.
 224 The dark current level in CIBER imagers is $\sim 0.1 e^-$
 225

² In the first and second CIBER flights, the longer wavelength
 band is centered at 1.56 μm , and thus it is named 1.6 μm band
 in previous CIBER publications (Bock et al. 2013; Zemcov et al.
 2014).

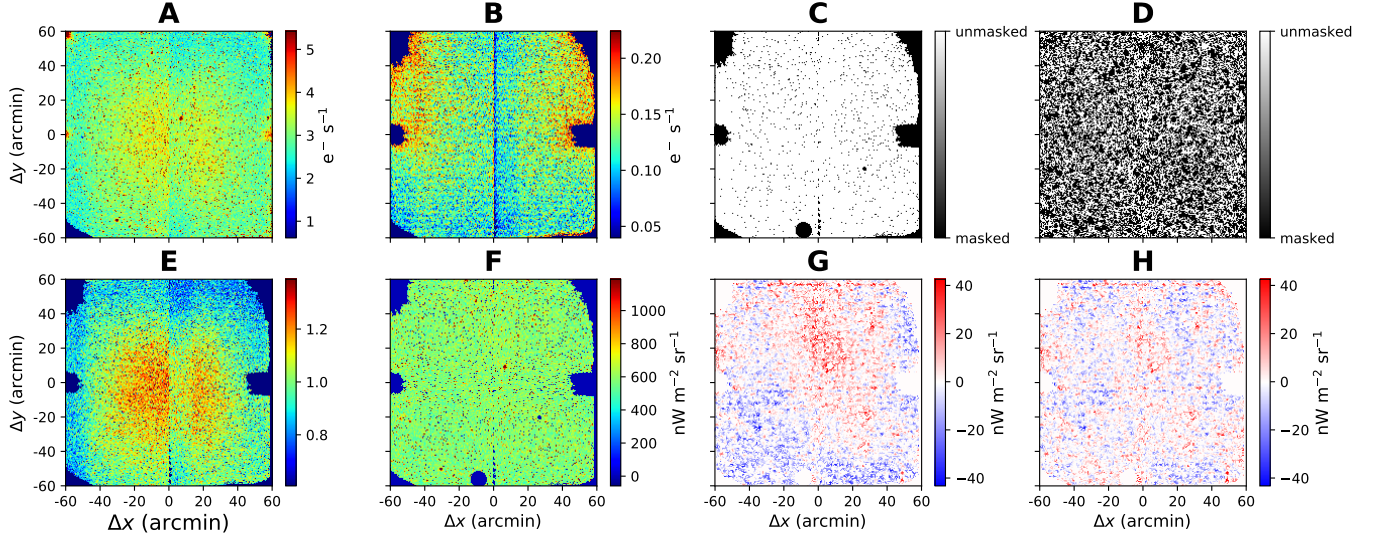


Figure 1. Images from the SWIRE field in the $1.1 \mu\text{m}$ band. A: the raw image of the photocurrent map. B: dark current template constructed from dark images before the flight. C: instrument mask encoding the pixels with fabrication defects, unusual photocurrents, and cosmic ray contamination. D: source mask for bright stars and galaxies in the 2MASS and Pan-STARRS catalogs. E: flat-field estimator from averaging the other four sky fields. F: raw image after dark current subtraction, flat field correction, and calibration. G: Image in Panel F after (constant) background removal and masking. This image is smoothed with a $\sigma = 35''$ Gaussian kernel to highlight large-scale fluctuations. H: Image in Panel G after subtracting a fitted 2-D polynomial, also shown smoothed with a $\sigma = 35''$ Gaussian kernel. Compared to Panel G, we see that the large-scale background fluctuations have been reduced after filtering. This is the final product of the data reduction pipeline.

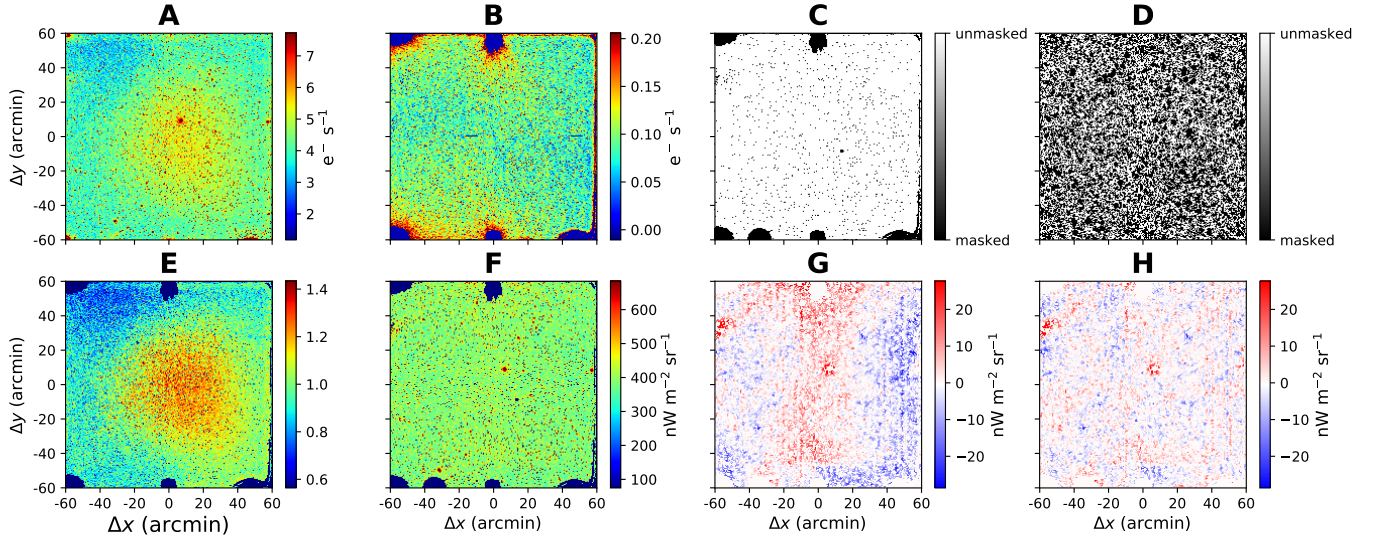


Figure 2. Same as Fig. 1 in the CIBER $1.8 \mu\text{m}$ band.

226 s^{-1} , less than 10 % of the sky brightness. Panel B of
 227 Fig. 1 and Fig. 2 show the dark current maps of CIBER
 228 1.1 and $1.8 \mu\text{m}$ bands, respectively.

229 3.3. Pixel Masks

230 We mask pixels that meet at least one of the follow-
 231 ing conditions: (1) a fabrication defect; (2) poor time-
 232 stream behavior; (3) abnormal photocurrents compared
 233 with other pixels; (4) a cosmic ray strike; or (5) being

234 on or close to bright point sources on the sky. The pix-
 235 els satisfying criteria (1)–(4) comprise the “instrument
 236 mask”, and a “source mask” is composed of pixels with
 237 condition (5).

238 3.3.1. Instrument Mask

239 Pixels with fabrication defects and significant mul-
 240 tiplexer glow are mostly distributed near the edges or
 241 corners of each quadrant on the detector arrays. They

exhibit pathologies in their photocurrent response, and can be found by comparison to the population of normal pixels. We perform a $3\text{-}\sigma$ clipping on stacked dark images (the same dataset used for a dark current template in Sec. 3.2) to identify these pixels.

During integration, some cosmic ray events or electronic transients leave a step feature in the time stream. We use a $100\text{-}\sigma$ clip on each time stream to pick out pixels that show these abrupt changes during an integration. Sometimes cosmic ray events also leave a comet-like structure on the array, and these regions are also masked. The union of the pathological pixel, time-stream masks, and cosmic ray masks form the instrument mask. In total, $\sim 10\%$ of pixels are removed by the instrument mask. Panel C of Fig. 1 and Fig. 2 show the instrument masks in the SWIRE field of 1.1 and 1.8 μm band, respectively.

3.3.2. Source Mask

To remove bright foreground stars and galaxies in our fields, we use position and brightness information from the Pan-STARRS and 2MASS catalogs (see Sec. 4 for details). We further derive source magnitudes in the two CIBER bands, $m_{1.1}$ and $m_{1.8}$, from these catalogs, as detailed in Sec. 4. We mask all point sources brighter than $m_{1.1} = 20$, choosing a masking radius for each source derived as follows. With the modeled instrument PSF (Sec. 7.3), the masking radius is chosen such that for each source, pixels with intensity brighter than $\nu I_{\nu}^{\text{th}} = 1 \text{ nW m}^{-2} \text{ sr}^{-1}$ in the 1.1 μm band are masked. This choice of threshold value removes $\sim 50\%$ of pixels in each field. We apply the same masking radius to 1.8 μm band sources. The same masking function is also applied to simulations to account for residual emission from bright sources outside the masks and the unmasked faint populations. Panel D of Fig. 1 and Fig. 2 show the SWIRE field source mask in the CIBER 1.1 and 1.8 μm bands, respectively.

The final mask we apply to the data is the union of the instrument mask and source mask. After applying these masks, we apply a final $3\text{-}\sigma$ pixel clipping mask to identify additional outliers not flagged through the other methods (e.g., from low-energy cosmic ray events or electronic transients).

3.4. Flat Fielding

CIBER images have a nonuniform response to a constant sky brightness across the detector array, known as the flat field response. For each CIBER field, the flat-field is estimated by averaging the dark-current-subtracted flight images of the other four sky fields.

A laboratory flat-field measurement was also taken before the flight using a field-filling integrating sphere,

a uniform radiance source with a solar spectrum (described in Bock et al. 2013). Ideally, this is a better approach to measure the flat field since the one derived from stacking flight images contains fluctuations from the other fields that will not average down completely due to the small number of images. However, we found the flat field from the integrating sphere is not consistent with the flight data on large spatial scales (see Zemcov et al. 2014), and therefore we do not use it in our analysis. The flat field estimator for the SWIRE field in CIBER 1.1 and 1.8 μm bands are shown in the Panel E of Fig. 1 and Fig. 2, respectively.

3.5. Surface Brightness Calibration

Throughout this work, we use $\text{nW m}^{-2} \text{ sr}^{-1}$ for the units of surface brightness (νI_{ν}). The calibration factor, C , that converts photocurrent ($\text{e}^{-} \text{ s}^{-1}$) to intensity ($\text{nW m}^{-2} \text{ sr}^{-1}$) is derived in the following steps:

1. Take the raw images, subtract the dark current template, correct for the flat field, and apply the instrument and source masks;
2. Subtract the mean photocurrent in the unmasked region.
3. For each star in the Pan-STARRS catalog, calculate the flux νF_{ν} in CIBER bands from $m_{1.1}$ and $m_{1.8}$.
4. Sum the photocurrent in a 5×5 stamp centered on the source position³.
5. Repeat step (3) and (4) for all the selected stars (see below) and take the average value of the flux ratio from (3) and (4) as the calibration factor C .

We select stars in the magnitude range $12.5 < m_{1.1} < 16$ for the 1.1 μm band, and $13.5 < m_{1.1} < 17$ for the 1.8 μm band. These magnitude ranges are chosen such that the brightest sources that saturate the detectors (even after non-linear correction) are excluded. Faint sources are not used because of their low signal-to-noise ratio. We use a different magnitude range for each band as they have different point source sensitivities. Panel F of Fig. 1 and Fig. 2 show the SWIRE field images masked by instrument masks at 1.1 and 1.8 μm , respectively, after flat fielding and calibration.

³ We have tested that using 3×3 , 5×5 , or 7×7 stamp size gives consistent results. Our beam size is approximately twice of the pixel size, so a 3×3 stamp already has enclosed most of the flux from a point source.

3.6. Background Removal

The total sky emission is composed of the EBL and various foreground components, including zodiacal light (ZL), diffuse galactic light (DGL), and integrated star light (ISL) from the Milky Way (Zemcov et al. 2014; Matsuura et al. 2017). ZL is the dominant foreground, approximately an order of magnitude brighter than the EBL (Matsuura et al. 2017). Nevertheless, with its smooth spatial distribution on degree scales, the ZL can be mostly removed by subtracting the mean sky brightness in each field. Panel G of Fig. 1 and Fig. 2 show the mean-subtracted and masked SWIRE images at 1.1 and 1.8 μm , respectively. To highlight the large-scale fluctuations, we smooth the images with a $\sigma = 35''$ Gaussian kernel.

3.7. Image Filtering

Although the ZL signal is smooth, a flat-field estimation error may induce a nonuniform ZL residual that cannot be removed by mean subtraction. This residual may dominate over cosmological fluctuations on large scales. Therefore, after removing the mean value in the image, we filter the images by fitting and subtracting a 3rd/5th order 2-D polynomial function for the 1.1/1.8 μm images to filter out any residual large-scale variations (Panel H of Fig. 1 and Fig. 2). The filtering will also suppress large-scale cosmological signals, and therefore the choice of polynomial order used for filtering is determined by optimizing the trade-off between the reduction of background fluctuations and the large-scale two-halo signal. The effect of filtering on the detected one-halo and galaxy extension terms is small, as our filtering removes fluctuations at a much larger scales than these signals, and the signal filtering is accounted for in simulations (see Sec. 9).

4. EXTERNAL CATALOGS

Throughout this work, we used several external source catalogs for (1) masking bright foreground sources (Sec. 3.3.2); (2) calibration (Sec. 3.5); (3) modeling the PSF by stacking bright stars in the fields (Sec. 7); and (4) selecting galaxies for stacking (Sec. 8).

To match the catalog sources to our data, we fit the astrometry coordinates of our images with the online software `nova.astrometry.net` (Lang et al. 2010). For each image, we solve for the astrometry in four quadrants separately to mitigate the effect of image distortion. Since there is a fixed $\sim 50''$ misalignment between the 1.1 and 1.8 μm images as they are produced by different telescopes, their astrometry is solved separately.

4.1. Pan-STARRS

We use the Pan-STARRS catalog (Chambers et al. 2016) for masking. Pan-STARRS covers all of the CIBER fields with a depth of $m \sim 20$ in the g, r, i, z, y bands. We query the source positions and magnitudes in all five Pan-STARRS bands from their DR1 `MeanObject` table, and derive $m_{1.1}$ and $m_{1.8}$ with the *LePhare* SED fitting software (Arnouts et al. 1999; Ilbert et al. 2006). We use sources that have a y band measurement and a quality flag (`qualityFlag` in `ObjectThin` table) that equals to 8 or 16 for masking.

4.2. 2MASS

Some bright stars are not included in the Pan-STARRS catalog, and thus we use the 2MASS (Skrutskie et al. 2006) Point Source Catalog (PSC) to get the complete point source list. For 2MASS sources, $m_{1.1}$ ($m_{1.8}$) is derived by linear extrapolation with the 2MASS photometric fluxes in J and H (H and K_s) bands, respectively. We also use bright stars in 2MASS for modeling the PSF (see Sec. 7).

4.3. SDSS

We use the Sloan Digital Sky Survey (SDSS) DR13 (Blanton et al. 2017) `PhotoObj` catalog to get the star/galaxy classification (“type” attribute 6–stars, 3–galaxies) and the galaxy photometric redshift (“Photoz” attribute) for sources in our fields. This information is essential for selecting target galaxies for stacking and inferring their redshift distribution (Sec. 8.1), as well as selecting stars for stacking to model the PSF (Sec. 7).

4.4. SWIRE Photometric Redshift Catalog

Rowan-Robinson et al. (2008, 2013) performed SED fitting on $\sim 10^6$ sources in the SWIRE field, based on optical and infrared photometric data from multiple surveys. This provides information on the stellar masses of our stacked galaxies for our analysis (see Sec. 8.2).

4.5. Gaia

Gaia DR2 (Gaia Collaboration et al. 2016, 2018) provides high-precision astrometry for stars in the Milky Way, which gives high-purity star samples used for both validating the PSF model (Sec. 7.2) and cleaning residual stars in the galaxy sample selected by SDSS (Sec. 8.1).

4.6. Nearby Cluster Catalog

Nearby galaxy clusters along the line of sight introduce extended emission in stacking, so we exclude galaxies that are close to nearby clusters (Sec. 8.1). We use the cluster catalog from Wen et al. (2012), which compiles $0.05 \leq z < 0.8$ galaxy clusters detected in SDSS-III

(Aihara et al. 2011). We also use the Abell cluster samples (Abell 1958) for local galaxy clusters. There are 7 Abell clusters and ~ 200 clusters from Wen et al. (2012) over the five CIBER fields.

5. SIMULATION CATALOG—MICECAT

In addition to the observed source catalogs, we make use of the MICECAT simulated galaxy catalog (Fosalba et al. 2015a,b; Hoffmann et al. 2015) to estimate the signal from galaxy clustering. MICECAT is a product of the N-body cosmological simulation MICE Grand Challenge run (MICE-GC), which has 70 billion dark matter particles in a $3072^3 \text{ Mpc}^3 h^{-3}$ cubic co-moving box. The dark matter halos are resolved down to $\sim 3 \times 10^{10} M_\odot h^{-1}$.

MICECAT is a mock catalog that simulates ideal observations of a 5000 deg^2 light cone covering $0 < z < 1.4$. MICECAT builds on MICE-GC by combining a halo occupation distribution (HOD) with subhalo abundance matching (SHAM) to calibrate to observed luminosity functions and clustering (Carretero et al. 2015). MICECAT simulates a mass-limited sample complete to $m_i \sim 22$ and $m_i \sim 24$ at $z \simeq 0.5$ and $z \simeq 0.9$, respectively (Crocce et al. 2015). The MICECAT mocks are large enough to permit us to generate up to $\sim 10^3$ independent CIBER field-sized ($2 \times 2 \text{ deg}^2$) mock catalogs. We use modeled magnitudes from MICECAT in Euclid NISP Y and H bands for CIBER $m_{1.1}$ and $m_{1.8}$, respectively, since the NISP filters are similar to the CIBER imager bands.

MICECAT simulates both central and satellite galaxies generated with its HOD+SHAM model, which allows us to model the linear (two-halo) and non-linear (one-halo) clustering in the stacking signal separately. We use the radial shapes derived from MICECAT stacking to fit the one-halo and two-halo amplitudes in our stacking data. Details on modeling galaxy clustering in the stacking signals are further described in Sec. 9.

6. STACKING

6.1. Sub-pixel Stacking

CIBER imager pixels under-sample the PSF, and therefore the surface brightness profile of individual sources is poorly resolved. However, given external source catalogs with high astrometric accuracy, we can stack on a sub-pixel basis and reconstruct the average source profile at scales finer than the native pixel size. This “sub-pixel stacking” technique has been used in previous CIBER imager analyses (Bock et al. 2013; Zemcov et al. 2014), and further investigated recently in the context of optimal photometry (Symons et al. 2021). We summarize the sub-pixel stacking procedure as follows:

1. Select a list of stacking target sources from external catalogs.
2. Re-grid each pixel into $N_{\text{sub}} \times N_{\text{sub}}$ sub-pixels (we use $N_{\text{sub}} = 10$ in this work). The intensities of all sub-pixels are assigned to the same value as the native pixel without interpolation.
3. For each source, unmask pixels associated with its source mask. Pixels masked due to nearby sources or from the instrument mask remain masked.
4. Crop an $N_{\text{size}} \times N_{\text{size}}$ (at sub-pixel resolution) stamp centered on the target source. We choose $N_{\text{size}} = 2401$ in this work, which corresponds to a $28' \times 28'$ stamp.
5. Repeat steps 3 and 4 for all target sources, average the stamps, and return the final stacked 2-D image $\Sigma_{\text{stack}}(\mathbf{r})$.

The stacked profile Σ_{stack} is a convolution of the intrinsic source profile, Σ_{src} , the instrument PSF (PSF_{instr})⁴, and the pixel function PSF_{pix} :

$$\begin{aligned} \Sigma_{\text{stack}}(\mathbf{r}) &= [\Sigma_{\text{src}}(\mathbf{r}) \otimes PSF_{\text{instr}}(\mathbf{r})] \otimes PSF_{\text{pix}}(\mathbf{r}) \\ &= \Sigma_{\text{src}}(\mathbf{r}) \otimes PSF_{\text{stack}}(\mathbf{r}), \end{aligned} \quad (1)$$

where $\mathbf{r} = (x, y)$ is a two-dimensional sub-pixel coordinate system with its origin at the stack center. We define the effective PSF as $PSF_{\text{stack}}(\mathbf{r}) \equiv PSF_{\text{instr}}(\mathbf{r}) \otimes PSF_{\text{pix}}(\mathbf{r})$. The pixel function accounts for the fact that sub-pixels retain the value of the original pixels, which is a convolution effect. The pixel function is a matrix with each element proportional to the counts where the sub-pixel and the center sub-pixel that contains the source are within the same native pixel. The position of the center sub-pixel within the native pixel is a uniform probability distribution, and therefore when stacking on a large number of sources, the pixel function converges to the analytic form (Symons et al. 2021):

$$PSF_{\text{pix}}(\mathbf{r}) = \begin{cases} (N_{\text{sub}} - x)(N_{\text{sub}} - y) & \text{if } |x|, |y| < N_{\text{sub}} \\ 0 & \text{otherwise} \end{cases} \quad (2)$$

As a practical matter, PSF_{pix} can be determined through simulations. $PSF_{\text{stack}}(\mathbf{r})$ can be measured by stacking stars in the field, where $\Sigma_{\text{src}}(\mathbf{r})$ is a delta function, so $\Sigma_{\text{stack}}(\mathbf{r}) = PSF_{\text{stack}}(\mathbf{r})$. Note that the expression in the second line of Eq. 1 implies that the intrinsic

⁴ Instrument PSF includes all effects from the optics, detector array, and pointing jitter during the integration.

517 profile $\Sigma_{\text{src}}(\mathbf{r})$ can be obtained from the stacked profile
518 $\Sigma_{\text{stack}}(\mathbf{r})$ with the knowledge of $PSF_{\text{stack}}(\mathbf{r})$, instead of
519 determining $PSF_{\text{instr}}(\mathbf{r})$.

520 We perform stacking and PSF modeling separately for
521 each field, since PSF_{instr} is slightly different across the
522 fields due to the varying pointing performance of the
523 altitude control system during each integration (c.f. top
524 panel of Fig. 5). After obtaining the 2-D stacked images,
525 we bin them into 25 logarithmically-spaced 1-D radial
526 bins. Within each bin, the number of stacked images on
527 each sub-pixel is used for weighting when calculating the
528 average profile in each radial bin. Note that the weight
529 is not the same across sub-pixels since the masks are
530 different for each stacked image.

531 6.2. Covariance Matrix of Stacking Profile

532 The covariance matrix of the binned 1-D radial
533 stacked profile is calculated with a jackknife resampling
534 technique. For each stack, we split sources into $N_J = 64$
535 sub-groups based on their spatial coordinates in the im-
536 age. The CIBER imager arrays have 1024×1024 pix-
537 els, and thus each sub-group corresponds to sources in
538 a 128×128 pixel sub-region on the array. The radial
539 profile of the k -th jackknife sample, Σ_{stack}^k , is obtained
540 from stacking on sources in all the other sub-regions,
541 and then the covariance matrix between radial bin (r_i ,
542 r_j) is given by

$$543 C_{\text{stack}}(r_i, r_j) = \frac{N_J - 1}{N_J} \sum_{k=1}^{N_J} [\Delta\Sigma_{\text{stack}}^k(r_i) \cdot \Delta\Sigma_{\text{stack}}^k(r_j)]$$

$$544 \Delta\Sigma_{\text{stack}}^k(r_i) \equiv \Sigma_{\text{stack}}^k(r_i) - \Sigma_{\text{stack}}(r_i)$$

$$545 \Delta\Sigma_{\text{stack}}^k(r_j) \equiv \Sigma_{\text{stack}}^k(r_j) - \Sigma_{\text{stack}}(r_j),$$
(3)

543 where Σ_{stack} is the average stacked profile of all of the
544 sub-regions.

545 One of our galaxy stacking samples (mag bin # 1 in
546 Sec. 8.1) has a small number of sources ($\ll 64$ for each
547 field), which makes the covariance estimation from the
548 jackknife method unstable. Therefore we perform boot-
549 strap resampling with $N_B = 1000$ realizations to calcu-
550 late the covariance for this case. In this bootstrap, we
551 obtain the radial profile of the k -th bootstrap sample,
552 Σ_{stack}^k , by stacking the same number of sources as the
553 original sample, but the sources are randomly selected
554 from the original sample with replacement. The covari-
555 ance matrix is then given by

$$556 C_{\text{stack}}(r_i, r_j) = \frac{1}{N_B - 1} \sum_{k=1}^{N_B} [\Delta\Sigma_{\text{stack}}^k(r_i) \cdot \Delta\Sigma_{\text{stack}}^k(r_j)].$$
(4)

556 In all the other cases, the covariance is derived from
557 jackknife instead of bootstrap resampling since it is nu-
558 merically expensive to perform a sufficient number of
559 bootstrap realizations given that we have hundreds or
560 thousands of galaxies per field in each stack. We assign
561 galaxies to sub-groups by their spatial positions instead
562 of randomly grouping them to account for large-scale
563 spatial fluctuations.

564 The first few radial bins within the CIBER $7''$ na-
565 tive pixel are highly correlated since all the sub-pixels
566 are assigned to the same value as the native pixel. We
567 also find a high correlation on large angular scales, as
568 the stacking signal is dominated by large-scale spatial
569 variations.

570 7. PSF MODELING

571 An accurate model for the PSF is essential for quan-
572 tifying the galaxy extension from stacking images. As
573 stars are point sources on the sky, we measure the PSF
574 of each field by stacking stars in the same CIBER field.
575 The radial profile of star stacks gives PSF_{stack} (Eq. 1),
576 which accounts for all effects that distribute the light
577 from a point source to the stacked profile, including
578 spreading by the instrument optical system and detec-
579 tors, pointing instability during integration, astrometry
580 uncertainties, and the pixel function PSF_{pix} . Since we
581 use bright stars in the CIBER fields to model the PSF,
582 the uncertainty on the PSF is subdominant to our galaxy
583 stacked profiles.

584 7.1. Modeling PSF_{stack}

585 Infrared detectors have a brightness-dependent PSF,
586 the so-called ‘‘brighter-fatter effect’’ (Hirata & Choi
587 2020). This nonlinearity makes brighter point sources
588 appear broader on the detector array than fainter ones.
589 To model PSF_{stack} robustly on both small and large
590 scales, we construct an overall star profile from three
591 brightness bins. For the core region ($r < 22''$), we
592 stack $13 < m_{1.1} < 14$ sources in the field; for inter-
593 mediate scales, $22'' < r < 40''$, we fit a slope to the
594 stacking profile of $9 < m_J^{2\text{MASS}} < 10$ sources; for outer
595 radii, we fit another slope to the stacking profile of the
596 brightest $4 < m_J^{2\text{MASS}} < 9$ sources, and connect the two
597 slopes at $r = 40''$ ($m_J^{2\text{MASS}}$ is the 2MASS J-band Vega
598 magnitude). The choice of magnitude bins and transi-
599 tion radii minimizes the error on all scales. At small
600 radii, using faint stars avoids detector nonlinearity, and
601 at large radii, bright stars provide better sensitivity to
602 the extended PSF. For the intermediate scales, we check
603 that the fitted slope from the three star stacking profiles
604 ($4 < m_J^{2\text{MASS}} < 9$, $9 < m_J^{2\text{MASS}} < 10$, $13 < m_{1.1} < 14$)
605 are statistically consistent. The top panel of Fig. 3 shows

606 PSF_{stack} from the SWIRE field in the $1.1 \mu\text{m}$ band. The
 607 top panel of Fig. 5 shows PSF_{stack} in all five fields in
 608 both bands. The slight variation across fields is due to
 609 the difference in the pointing stability during each integra-
 610 tion, but such motion is common to all sources within
 611 an integration.

7.2. Validating PSF_{stack}

613 To validate that our PSF model is applicable to the
 614 fainter sources of interest, we perform a consistency test
 615 by stacking on stars in the Gaia catalog within the same
 616 magnitude range as our stacked galaxy samples ($16 <$
 617 $m_{1.1} < 20$), and compare these star stacking profiles
 618 with our PSF_{stack} model.

619 To get a clean star sample free of galaxies, we apply
 620 the following criteria for selecting stars from Gaia:

- 621 1. The source has a parallax measurement $> 2 \times 10^{-4}$
 622 mas (i.e., distance < 5 kpc).
- 623 2. No astrometric excess noise is reported in the Gaia
 624 catalog (`astrometric_excess_noise` = 0). Large
 625 astrometric excess noise implies the source might
 626 be extended rather than a point source.
- 627 3. No SDSS galaxies within $0.7''$ (sub-pixel grid size)
 628 radius around the source.
- 629 4. We classify SDSS stars and galaxies using 10 pairs
 630 of magnitude differences between the five Pan-
 631 STARRS photometric magnitudes (g , r , i , z , and
 632 y bands), rejecting sources if they are classified as
 633 galaxies by our trained model.

634 After selecting stars with the above conditions from the
 635 the Gaia catalog, we stack them in four equally-spaced
 636 magnitude bins between $16 < m_{1.1} < 20$, and compare
 637 their stacking profile with the PSF_{stack} model. These
 638 stars span the same brightness range used for galaxy
 639 stacking. We down-sample original 25 radial bins to 15
 640 bins (7 bins for $16 < m_{1.1} < 17$ case), following the same
 641 binning used for the galaxy stacking profile (Sec. 8.4).
 642 The results in the $1.1 \mu\text{m}$ band SWIRE field are shown
 643 on the bottom panel of Fig. 3. In Fig. 4 we show the
 644 difference of Gaia star stacks and the PSF_{stack} model.
 645 The errors are propagated from the covariance of the
 646 PSF_{stack} model and Gaia star stacks. We also show the
 647 χ^2 values and the corresponding probability to exceed
 648 (PTE) on all five CIBER fields in both bands. The PSF
 649 model shows excellent agreement with the star stacks.

7.3. Modeling PSF_{instr}

651 Although knowledge of the instrument PSF is not re-
 652 quired for reconstructing the source profile Σ_{src} from

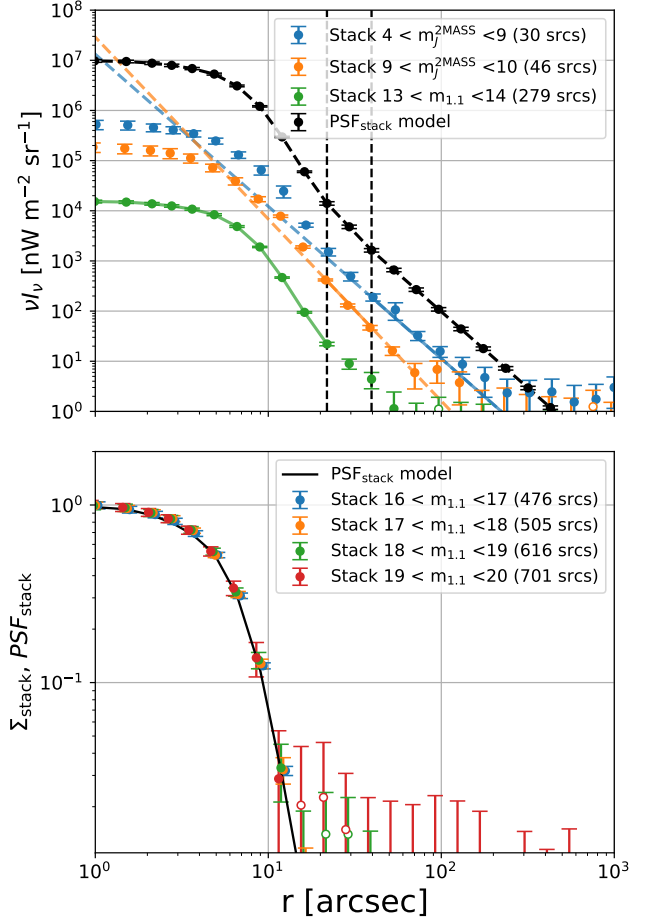


Figure 3. We illustrate the process of constructing and validating the $PSF_{\text{stack}}(r)$ model, in the $1.1 \mu\text{m}$ band SWIRE field. Top: star stacking profile in three different brightness bins (blue, orange, and green), and the combined $PSF_{\text{stack}}(r)$ model (black dashed curve) derived from splicing these three stacking profiles together at the radii marked by the black vertical dashed lines. The black data points show the binned $PSF_{\text{stack}}(r)$ and the error bars propagated from their original star stacks. The filled data points and the three colored solid curves are the data used in the $PSF_{\text{stack}}(r)$ model. Bottom: comparison of the $PSF_{\text{stack}}(r)$ model with the stacking profiles from fainter stars selected from Gaia. The four chosen brightness bins match the ones used in galaxy stacking. The $PSF_{\text{stack}}(r)$ model agrees closely with the star stacking profiles, as shown in Fig. 4.

653 the stacking profile $\Sigma_{\text{stack}}, PSF_{\text{instr}}$ is still needed when
 654 we model the clustering signal from a simulated catalog
 655 (Sec. 9), where we make mock galaxy images using the
 656 CIBER PSF and pixel gridding. PSF_{instr} is also useful
 657 for determining the masking radius for bright sources
 658 (Sec. 3.3.2).

659 PSF_{instr} is modeled as follows: first, we deconvolve
 660 $PSF_{\text{pix}}(\mathbf{r})$ (Eq. 2) from the $PSF_{\text{stack}}(\mathbf{r})$ model with 10
 661 iterations of the Richardson-Lucy deconvolution algo-

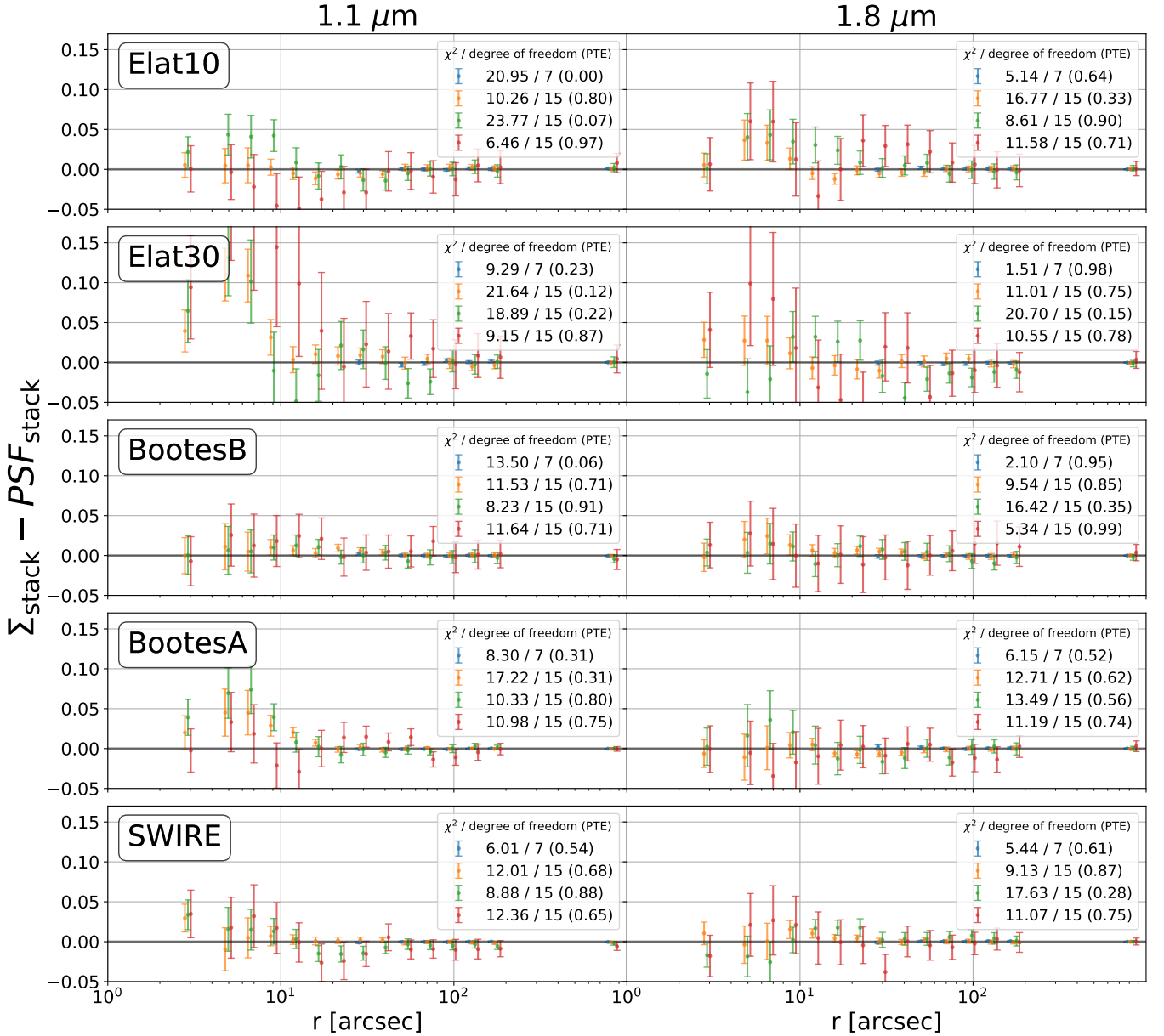


Figure 4. The difference of the $PSF_{\text{stack}}(r)$ model and the star stacking profiles in all five CIBER fields in the 1.1 μm (left) and 1.8 (right) μm bands ($16 < m_{1.1} < 17$ (blue), $17 < m_{1.1} < 18$ (orange), $18 < m_{1.1} < 19$ (green), and $19 < m_{1.1} < 20$ (red)). The χ^2 values and their corresponding PTE given in the legend are consistent with the model. The degrees of freedom for each case is simply the number of radial bins. Open circles in the top and middle panels represent negative data points.

662 rithm (Richardson 1972; Lucy 1974). The deconvolu-
 663 tion is unstable at large radii due to noise fluctuations.
 664 To get a smooth model for PSF_{instr} , we fit a β model
 665 (Cavaliere & Fusco-Femiano 1978) to the 1-D profile of
 666 the deconvolved image:

$$PSF_{\text{instr}}(r) = \left(1 + \left(\frac{r}{r_c}\right)^2\right)^{-3\beta/2}. \quad (5)$$

667 Though not physically motivated, we find β model is
 668 a good empirical description of the extended PSF, and

669 requires only two free parameters to achieve acceptable
 670 goodness of fit for every PSF_{stack} .

671 The bottom panel of Fig. 5 illustrates this proce-
 672 dure in the 1.1 μm band of the SWIRE field. The
 673 PSF_{stack} model, obtained from star stacks in three dif-
 674 ferent brightness bins, matches the β model of PSF_{instr}
 675 convolved with the pixel function PSF_{pix} (Eq. 2). Our
 676 instrument PSF has comparable size to a pixel (FWHM
 677 $\sim 7''$).

8. GALAXY STACKING

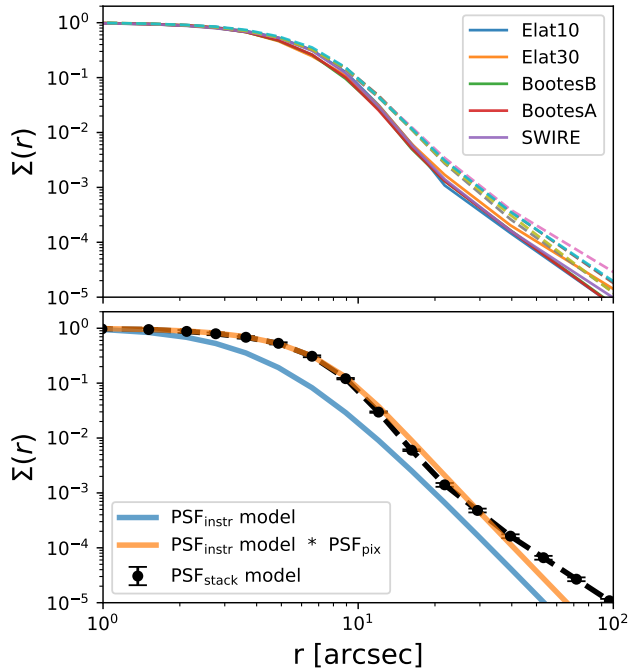


Figure 5. Top: PSF_{stack} model for each of the five fields in the $1.1 \mu\text{m}$ (solid) and $1.8 \mu\text{m}$ (dashed) bands. The variation across fields is due to the difference in pointing stability. Bottom: demonstration of the PSF_{instr} reconstruction process. Black data points show the PSF_{stack} model in the $1.1 \mu\text{m}$ band SWIRE field, derived from splicing the star stacking profile in three different brightness bins (c.f. Fig. 3 top panel). The blue line is the PSF_{instr} model derived from fitting a β model to PSF_{stack} after deconvolving PSF_{pix} with the Richardson-Lucy deconvolution algorithm. The orange line shows the convolution of PSF_{instr} with PSF_{pix} matching the PSF_{stack} model, as a consistency check. Our model for PSF_{instr} is in agreement with data for $r \lesssim 30''$. Our analysis is not susceptible to the moderate error at larger radii, as PSF_{instr} is only used for characterizing the clustering signal from nearby galaxies.

We stack galaxies within magnitude ranges $16 < m_{1.1} < 20$, divided into several sub-samples spanning $\Delta m_{1.1} = 1$. Our choice of magnitude bins optimizes the SNR on the stacks, giving sufficient sample sizes for each source brightness.

8.1. Source Selection Criteria

The stacking galaxy samples are selected from the SDSS catalog in the CIBER fields. To mitigate systematic effects from confusion, nearby clusters, or misclassified stars in the sample, we reject sources if they meet any of the following criteria:

- Sources are not labeled as galaxies in the SDSS catalog, i.e., the “type” attribute in the SDSS PhotoObj table is not equal to 3.

- Sources are located in the instrument mask.
- Other Pan-STARRS sources exist in the same CIBER pixel.
- The SDSS photometric redshift is less than 0.15. This criteria prevents nearby galaxies from introducing substantial power on large angular scales that would otherwise mimic the clustering signal.
- Sources have nearby Gaia counterparts within $0.7''$, i.e., the size of the sub-pixel used in our stacking. These sources are likely to be stars that are misclassified as galaxies in the SDSS catalog.
- Sources are within (1) a $500''$ radius of any galaxy cluster in Abell (1958) (Sec 4.6); or (2) R_{200} of any galaxy cluster with halo mass $M_h > 10^{14} M_\odot$ or redshift $z < 0.15$ in the SDSS cluster catalog (Wen et al. (2012), Sec 4.6). Approximately 10% of the sky area in each field is excluded by this condition.

The last condition mitigates contamination from nearby clusters along the line of sight, since they have structures spanning large angular scales, which will produce spurious large-scale extended signals in the stack. Furthermore, as we do not have information on whether a galaxy in SDSS is a member of a large galaxy cluster, the criteria also excludes cluster members from our stacking sample. Stacking on cluster members introduces extra non-linear one-halo clustering that can overwhelm the linear two-halo clustering signal on large scales.

To quantify the effect of applying this condition, we generate a mock CIBER map from the MICECAT catalog, implementing the same strategies described above to select sources, and stacking on the mock maps to measure the one- and two-halo clustering signals (see Sec. 9 for a detailed description of stacking with MICECAT-generated maps). We tested over a range of halo mass and redshift for selecting clusters, and found that excluding sources around clusters with $M_h > 10^{14} M_\odot$ (or redshift $z < 0.15$) can effectively reduce the one-halo clustering signal on large scales without losing a significant number of sources. For example, for the magnitude range of interest in this work (see Sec. 8.2), we can reduce the one-halo power by $\sim 3 - 5\times$ at 100 arcsec radius just by excluding galaxies near clusters following our criteria.

8.2. Stacking Sub-samples

For the SDSS galaxies within $16 < m_{1.1} < 20$ that survive all the selection criteria above, we split the sources

into two sets. The first set is based on 1.1 μm flux in four bins: $16 < m_{1.1} < 17$, $17 < m_{1.1} < 18$, $18 < m_{1.1} < 19$, and $19 < m_{1.1} < 20$. Hereafter, these four bins are named “mag bin # 1”, “mag bin # 2”, “mag bin # 3”, and “mag bin # 4”, respectively. In addition, we also define a “total stack” with all $17 < m_{1.1} < 20$ sources to achieve better large-scale sensitivity.

The second set is defined by both the 1.1 μm apparent magnitude $m_{1.1}$ and the absolute magnitude $M_{1.1}$: $M_{1.1} = m_{1.1} - DM(z) + 2.5\log_{10}(1+z)$, where DM is the distance modulus, using SDSS photometric redshifts. The absolute flux serves as a proxy for galaxy size. Galaxies with comparable absolute flux have similar bolometric luminosity, which is correlated with stellar mass, star formation rate, etc. We use these samples to explore the dependence of our results on different galaxy properties. Since the sets approximately correspond to three higher and two lower stellar mass populations, with different redshift distributions, we call them “high-M/low-z”, “high-M/med-z”, “high-M/high-z”, “low-M/low-z”, and “low-M/med-z”.

In the SWIRE field, we have additional information from a photometric redshift catalog (Rowan-Robinson et al. 2013) based on an SED fit to each galaxy. As the stacked samples from each field are selected with the same criteria, we can assume the galaxy property distributions in the SWIRE field are the same as other fields, and thus infer the stellar mass distribution over all five fields. The $\log M_*$ column in Table 2 lists the median and 68% interval stellar mass in the SWIRE field samples from the Rowan-Robinson et al. (2013) catalog. The stellar masses of our samples span from $\sim 10^{10.5}$ to $10^{12} M_\odot$, i.e., $\sim L_*$ galaxies at this redshift (Muzzin et al. 2013). In addition, with the stellar mass distribution, we infer the host halo mass of our samples using the mean stellar-to-halo mass relation given by Zu & Mandelbaum (2015), which connects the halo mass to stellar mass with galaxy clustering and lensing measurements. We also derive the corresponding virial radius, R_{200} (in physical and angular units), in Table 2. The virial radius is calculated from $R_{200} = [3M_h/(4\pi \cdot 200\rho_c)]^{1/3}$, where ρ_c is the critical density.

We note that by selecting galaxies based on absolute or apparent fluxes, our samples will include both central and satellite galaxies. We infer the fraction of central galaxies, f_{cen} , in each sub-sample from MICECAT by applying the same selection criteria from a MICECAT simulation (i.e., observed magnitude, absolute magnitude and redshift cuts, and excluding sources close to nearby clusters). The distribution of redshift, stellar mass, halo mass, virial radius, and f_{cen} of our sub-samples are summarized in Fig. 6 and Table 2.

8.3. Galaxy Stacking Profile

We calculate 1-D radial profiles from galaxy stacks by averaging pixels in concentric annuli, as shown in Fig. 7 and Fig. 8. For comparison, we also plot the expected profile of stacked point sources, PSF_{stack} , scaled to match the first radial bin of the stacked galaxy profile. In all cases, the galaxy profiles are clearly broader than the PSF_{stack} profile.

8.4. Excess Profile

We define an “excess profile” $\Sigma_{\text{ex}}(r)$ as follows:

$$\Sigma_{\text{ex}}(r) = \Sigma_{\text{stack}}(r) - A \cdot PSF_{\text{stack}}(r), \quad (6)$$

where the normalization factor A is chosen such that PSF_{stack} matches Σ_{stack} at the innermost radial bin r_1 , and thus by construction, $\Sigma_{\text{ex}}(r_1) = 0$, and $A \equiv \Sigma_{\text{stack}}(r_1)/PSF_{\text{stack}}(r_1)$.

Since the excess profile is fixed at r_1 , the uncertainties on the galaxy profile and the PSF profile at r_1 have to be accounted for by propagating this error to the other radial bins, and thus the excess profile covariance is given by

$$C_{\text{ex}} = \Sigma_{\text{stack}}(r_1)^2 [C_{\text{norm}}(C_{\text{stack}}) + C_{\text{norm}}(C_{\text{PSF}})], \quad (7)$$

where C_{PSF} and C_{stack} are the covariance of PSF_{stack} and Σ_{stack} , respectively, and

$$\begin{aligned} C_{\text{norm}} & \left(C, \frac{\Sigma_{\text{stack}}(r_i)}{\Sigma_{\text{stack}}(r_1)}, \frac{\Sigma_{\text{stack}}(r_j)}{\Sigma_{\text{stack}}(r_1)} \right) \\ & = \frac{\Sigma_{\text{stack}}(r_i)\Sigma_{\text{stack}}(r_j)}{\Sigma_{\text{stack}}(r_1)^2} \\ & \left[\frac{C(r_i, r_j)}{\Sigma_{\text{stack}}(r_i)\Sigma_{\text{stack}}(r_j)} - \frac{C(r_i, r_1)}{\Sigma_{\text{stack}}(r_i)\Sigma_{\text{stack}}(r_1)} \right. \\ & \quad \left. - \frac{C(r_j, r_1)}{\Sigma_{\text{stack}}(r_j)\Sigma_{\text{stack}}(r_1)} + \frac{C(r_1, r_1)}{\Sigma_{\text{stack}}(r_1)^2} \right] \end{aligned} \quad (8)$$

is the covariance for the normalized profile that follows from the product rule for derivatives.

To fit a model to the measured Σ_{ex} , we also need the inverse of C_{ex} . However, C_{ex} is close to singular since our radial bins are highly correlated. Therefore, we reduce the original 25 radial bins to 15 bins by combining highly correlated bins in the inner and outer regions⁵. After this down-sampling, we derive the inverse covariance estimator by

$$C_{\text{ex}}^{-1} = \frac{N_J - N_{\text{bin}} - 2}{N_J - 1} C_{\text{ex}}^{*-1}, \quad (9)$$

⁵ Mag bin # 1 is down-sampled to 7 radial bins as its degree of freedom is limited by the small number of stacked sources.

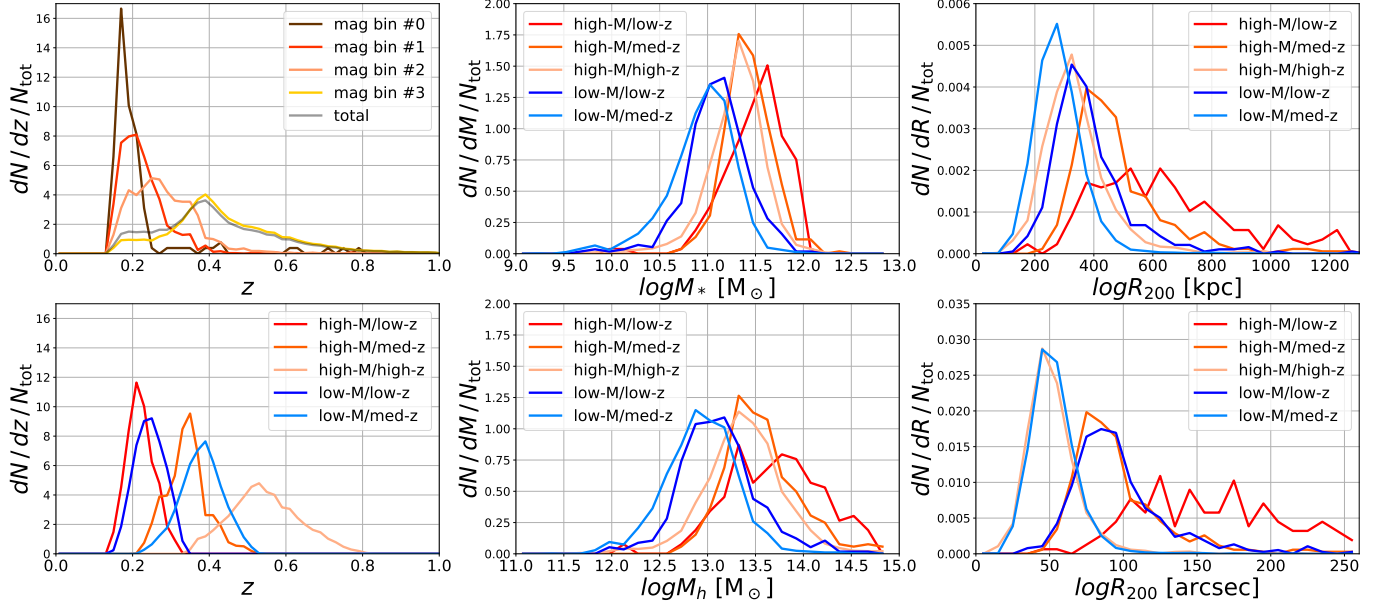


Figure 6. Left: redshift distributions of the 10 galaxy sub-samples used for stacking. The redshifts are derived from SDSS photometry. Middle-top: stellar mass distributions for the 5 apparent and absolute magnitude selected bins. The stellar masses are inferred from Rowan-Robinson et al. (2013) for the SWIRE field. Middle-bottom: halo mass distributions in 5 apparent and absolute magnitude selected bins, modeled by applying stellar-to-halo mass relation from Zu & Mandelbaum (2015). Right: distributions of virial radius in physical (top) and observed angular (bottom) units. For visualization purposes, all curves are normalized by the total number of sources in each sub-sample (N_{tot}).

823 where $N_j = 64$, the number of sub-groups used for estimating
 824 covariance, and the number of bins $N_{\text{bin}} = 15$.
 825 C_{ex}^{*-1} is the direct inverse of the C_{ex} matrix, and the
 826 pre-factor in Eq. 9 de-biases the inverse covariance estimator,
 827 as our covariance matrix is derived from our data (Hartlap et al. 2007)⁶.

828 While we have high sensitivity on the small radial bins of both
 829 the galaxy stacked profiles and the PSF model, the A value has
 830 minimal dependency on the radius chosen for normalization, and
 831 the uncertainty of normalization has been accounted by the covariance
 832 (Eq. 7), and thus our model parameter inference (Sec. 9) does not
 833 depend on the definition of the excess profile.
 834

835 We present field-averaged excess profiles in Fig. 9. Note that the
 836 field-averaged excess profile is only plotted for visualization purposes,
 837 since the field-to-field PSF variation must be explicitly accounted
 838 in parameter fitting.
 839

841 9. MODELING THE GALAXY PROFILES

842 We model the galaxy profile with three components as follows. We
 843 start by decomposing the stacked profile in image space (Sec. 9.1),
 844 define fitted profiles (Sec. 9.2), and introduce our model for each
 845 component of the stack

846 (Sec. 9.3). Finally, we describe the model fitting procedure in
 847 Sec. 9.4.

848 9.1. Components in Image Space

849 The raw CIBER image, I_{raw} , can be expressed as⁷

$$850 \begin{aligned} I_{\text{raw}}(\mathbf{x}) = & [I_{\text{sig}}(\mathbf{x}) + I_{\text{LoS}}(\mathbf{x})] \otimes PSF_{\text{instr}}(\mathbf{r}) \cdot FF(\mathbf{x}) \\ & + I_{\text{DC}}(\mathbf{x}) + I_{\text{n}}(\mathbf{x}), \end{aligned} \quad (10)$$

851 where \mathbf{x} is the 2-D pixel coordinate, FF is the flat-field gain,
 852 I_{DC} is the dark current map, and I_{n} is the read noise plus
 853 photon noise. The sky emission is decomposed into I_{sig} and
 854 I_{LoS} terms, where the first term accounts for the signal associated
 855 with stacked galaxies, and I_{LoS} represents uncorrelated emission
 856 from all other sources along the line of sight, including Galactic
 857 foregrounds.

858 After dark current subtraction and flat-field correction, we retrieve
 859 I'_{raw} :

$$860 I'_{\text{raw}}(\mathbf{x}) = [I_{\text{sig}}(\mathbf{x}) + I_{\text{LoS}}(\mathbf{x})] \otimes PSF_{\text{instr}}(\mathbf{r}) + I'_{\text{n}}(\mathbf{x}), \quad (11)$$

861 where $I'_{\text{n}}(\mathbf{x}) = I_{\text{n}}(\mathbf{x})/FF(\mathbf{x})$, the instrument noise divided
 862 by the flat-field response. For simplicity, we ignore

⁶ For mag bin # 1, $N_{\text{bin}} = 7$, and $N_j = 64$ is replaced by $N_B = 1000$ since we use bootstrap resampling method in this case.

⁷ For clarification, \mathbf{x} denotes 2-D coordinate on CIBER images, and \mathbf{r} represents the coordinate that has origin at the source center, which is used in PSF_{instr} and stacked maps. Since we only consider 1-D radially averaged profile, \mathbf{r} is replaced by 1-D variable “ r ”.

Table 2. Summary of the properties on each stacked galaxy sub-sample with the +/- values indicating the 68% interval ranges.

Name	Selection Criteria	N_{gal}	z	$\log M_* [M_{\odot}]$	$\log M_h [M_{\odot}]$	$R_{200} [\text{kpc}]$	$R_{200} [\text{arcsec}]$	f_{cen}
mag bin #1	$16 < m_{1.1} < 17$	129	$0.18^{+0.04}_{-0.02}$	$11.6^{+0.3}_{-0.3}$	$13.8^{+0.5}_{-0.4}$	679^{+325}_{-181}	215^{+103}_{-57}	0.65
mag bin #2	$17 < m_{1.1} < 18$	1173	$0.21^{+0.07}_{-0.04}$	$11.5^{+0.3}_{-0.4}$	$13.7^{+0.6}_{-0.6}$	584^{+357}_{-215}	163^{+100}_{-60}	0.67
mag bin #3	$18 < m_{1.1} < 19$	3465	$0.27^{+0.09}_{-0.07}$	$11.2^{+0.4}_{-0.3}$	$13.3^{+0.5}_{-0.4}$	401^{+178}_{-116}	94^{+42}_{-27}	0.62
mag bin #4	$19 < m_{1.1} < 20$	31157	$0.42^{+0.17}_{-0.11}$	$11.1^{+0.3}_{-0.5}$	$13.0^{+0.5}_{-0.5}$	285^{+127}_{-86}	50^{+22}_{-15}	0.63
total	$17 < m_{1.1} < 20$	35795	$0.40^{+0.17}_{-0.14}$	$11.1^{+0.3}_{-0.4}$	$13.1^{+0.5}_{-0.5}$	302^{+135}_{-93}	55^{+24}_{-17}	0.63
high-M/low-z	$17 < m_{1.1} < 18$ $-23 < M_{1.1} < -22$	743	$0.22^{+0.04}_{-0.03}$	$11.6^{+0.2}_{-0.4}$	$13.7^{+0.5}_{-0.5}$	608^{+266}_{-201}	168^{+73}_{-55}	0.66
high-M/med-z	$18 < m_{1.1} < 19$ $-23 < M_{1.1} < -22$	1274	$0.34^{+0.05}_{-0.05}$	$11.4^{+0.3}_{-0.2}$	$13.5^{+0.4}_{-0.3}$	447^{+157}_{-94}	89^{+31}_{-19}	0.62
high-M/high-z	$19 < m_{1.1} < 20$ $-23 < M_{1.1} < -22$	10916	$0.54^{+0.10}_{-0.09}$	$11.3^{+0.3}_{-0.3}$	$13.4^{+0.3}_{-0.4}$	325^{+100}_{-82}	50^{+15}_{-13}	0.66
low-M/low-z	$18 < m_{1.1} < 19$ $-22 < M_{1.1} < -21$	1645	$0.24^{+0.05}_{-0.03}$	$11.1^{+0.3}_{-0.2}$	$13.1^{+0.4}_{-0.3}$	359^{+129}_{-78}	90^{+33}_{-20}	0.57
low-M/med-z	$19 < m_{1.1} < 20$ $-22 < M_{1.1} < -21$	14730	$0.38^{+0.05}_{-0.05}$	$11.0^{+0.2}_{-0.4}$	$12.9^{+0.3}_{-0.4}$	275^{+78}_{-67}	51^{+15}_{-13}	0.58

NOTE— N_{gal} is the total number of galaxies across five CIBER fields in each sub-sample, and the redshifts z are derived from SDSS photometry. The quantities on the left side of the double vertical line are derived from a partial set of samples or external catalogs for the sources used in stacks. We infer M_* by matching SWIRE field sources to the catalog from Rowan-Robinson et al. (2013), assuming the same M_* distribution applies to the other four fields. **The halo mass and the virial radius are derived with the stellar-to-halo mass relation from Zu & Mandelbaum (2015). The fraction of central galaxies (f_{cen}) is derived by applying the same cuts to a simulated catalog from MICECAT.**

861 the error in the flat-field estimator in Eq. 11. In practice, the flat-field estimation uncertainties will not bias
862 the stacking results as they are not correlated with individual stacked sources, and the effect on the covariance
863 is accounted by the Jackknife method (see Sec. 6.2). We define the mask $M(\mathbf{x})$ as a binary function set to zero
864 at masked pixels, and one otherwise. The filtered map is expressed with $\mathcal{F}[I'_{\text{raw}}(\mathbf{x}), M(\mathbf{x})]$, which is a function
865 of the input map $I'_{\text{raw}}(\mathbf{x})$ and mask $M(\mathbf{x})$. As described in Sec. 3.7, we choose \mathcal{F} to be a 3rd (1.1 μm)/5th (1.8
866 μm) order 2-D polynomial function fitted to the masked I'_{raw} map⁸. The image used for stacking I_{map} can thus
867 be written as

$$\begin{aligned}
I_{\text{map}}(\mathbf{x}) &= I'_{\text{raw}}(\mathbf{x})M(\mathbf{x}) - \mathcal{F}[I'_{\text{raw}}(\mathbf{x}), M(\mathbf{x})]M(\mathbf{x}) \\
&= I_{\text{map}}^{\text{sig}}(\mathbf{x}) + I_{\text{map}}^{\text{LoS}}(\mathbf{x}) + I_{\text{map}}^{\text{n}}(\mathbf{x}),
\end{aligned}
\tag{12}$$

874 where

$$\begin{aligned}
I_{\text{map}}^{\text{sig}}(\mathbf{x}) &= [I_{\text{sig}}(\mathbf{x}) \otimes \text{PSF}_{\text{instr}}(\mathbf{r})]M(\mathbf{x}) \\
&- \mathcal{F}[I_{\text{sig}}(\mathbf{x}) \otimes \text{PSF}_{\text{instr}}(\mathbf{r}), M(\mathbf{x})]M(\mathbf{x}),
\end{aligned}
\tag{13}$$

⁸ Note that the filter map \mathcal{F} can be decomposed into the sum
of three filter maps because the polynomial fitting is a linear
operation, i.e., given two maps $A(\mathbf{x})$ and $B(\mathbf{x})$, and a mask $M(\mathbf{x})$,
 $\mathcal{F}[A(\mathbf{x}) + B(\mathbf{x}), M(\mathbf{x})] = \mathcal{F}[A(\mathbf{x}), M(\mathbf{x})] + \mathcal{F}[B(\mathbf{x}), M(\mathbf{x})]$.

$$\begin{aligned}
I_{\text{map}}^{\text{LoS}}(\mathbf{x}) &= [I_{\text{LoS}}(\mathbf{x}) \otimes \text{PSF}_{\text{instr}}(\mathbf{r})]M(\mathbf{x}) \\
&- \mathcal{F}[I_{\text{LoS}}(\mathbf{x}) \otimes \text{PSF}_{\text{instr}}(\mathbf{r}), M(\mathbf{x})]M(\mathbf{x}),
\end{aligned}
\tag{14}$$

875 and

$$\begin{aligned}
I_{\text{map}}^{\text{n}}(\mathbf{x}) &= I'_{\text{n}}(\mathbf{x})M(\mathbf{x}) \\
&- \mathcal{F}[I'_{\text{n}}(\mathbf{x}), M(\mathbf{x})]M(\mathbf{x}).
\end{aligned}
\tag{15}$$

9.2. Components in the Stack

877 The stacked profile Σ_{stack} can be expressed as the sum
878 of stacks on the three maps in Eq. 12:

$$\Sigma_{\text{stack}}(r) = \Sigma_{\text{stack}}^{\text{sig}}(r) + \Sigma_{\text{stack}}^{\text{LoS}}(r) + \Sigma_{\text{stack}}^{\text{n}}(r).
\tag{16}$$

879 The last two terms can be ignored in modeling since
880 they are uncorrelated with the stacked sources, so
881 $\langle \Sigma_{\text{stack}}^{\text{LoS}}(r) \rangle = \langle \Sigma_{\text{stack}}^{\text{n}}(r) \rangle = 0$.

882 We model the stacked galaxy profile as

$$\begin{aligned}
\Sigma_{\text{stack}}^{\text{sig}}(r) &= [\Sigma_{\text{stack}}^{\text{gal}}(r) + \Sigma_{\text{stack}}^{\text{1h}}(r) + \Sigma_{\text{stack}}^{\text{2h}}(r)] \\
&- \Sigma_{\text{stack}}^{\mathcal{F}}(r),
\end{aligned}
\tag{17}$$

886 where the first three terms are the signal terms, and the
last term is the filtered signal map in Eq. 13. The galaxy
profile term, $\Sigma_{\text{stack}}^{\text{gal}}$, represents the intrinsic galaxy profile,
which includes the galaxy shape and the extended

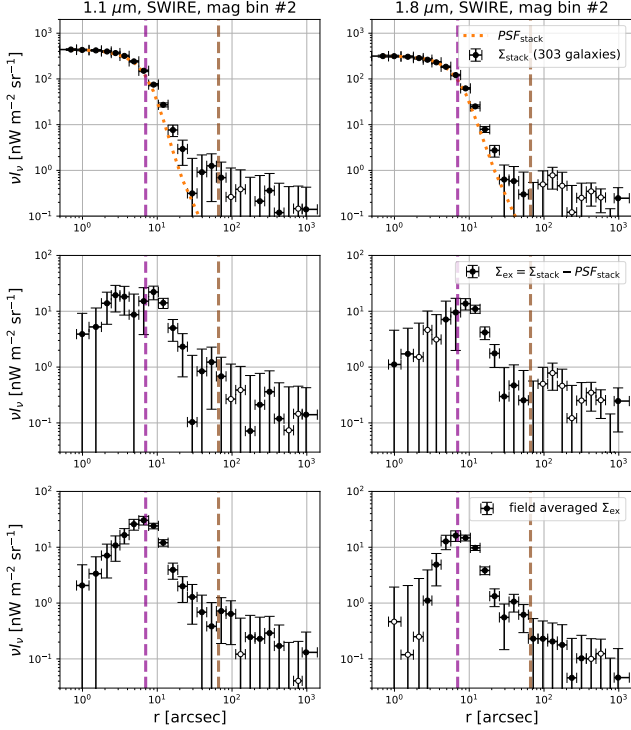


Figure 7. The stacked galaxy radial profile from the SWIRE field mag bin #2 in the 1.1 (left) and 1.8 μm (right) bands. Top: galaxy stacked profile Σ_{stack} (black) and PSF_{stack} model (orange dashed), scaled to match the innermost radial bin of Σ_{stack} . The error bars give the diagonal element of the covariance matrix derived by the Jackknife method (described in Sec. 3). Middle: the excess profile (Σ_{ex} , Eq. 6) for the case shown in the top row. The excess is defined as the difference between the galaxy stacked profile and the PSF_{stack} model, i.e., the difference of the black data from the orange curve in the top row. Bottom: the field-averaged excess profile Σ_{ex} for mag bin #2, derived from the weighted average of the excess profile in the five individual fields. The improved sensitivity from combining fields can be seen compared to the middle row. The purple and brown dashed lines mark the pixel size and the median R_{200} values inferred from MICECAT, respectively. Open circles in all the plots represent negative values.

stellar halo. We decompose the galaxy profile term, $\Sigma_{\text{stack}}^{\text{gal}}$, into “core” and “extended” parts:

$$\Sigma_{\text{stack}}^{\text{gal}}(r) = \Sigma_{\text{core}}^{\text{gal}}(r) + \Sigma_{\text{ext}}^{\text{gal}}(r), \quad (18)$$

where the core component is the integrated emission of the PSF_{stack} fitted to the stacking profile, i.e., the $A \cdot PSF_{\text{stack}}$ term in Eq. 6, and the extended component is the rest of the galaxy emission:

$$\begin{aligned} \Sigma_{\text{core}}^{\text{gal}}(r) &= \Sigma_{\text{stack}}(r) - \Sigma_{\text{ex}}(r), \\ \Sigma_{\text{ext}}^{\text{gal}}(r) &= \Sigma_{\text{ex}}(r) \\ &\quad - [\Sigma_{\text{stack}}^{1\text{h}}(r) + \Sigma_{\text{stack}}^{2\text{h}}(r) - \Sigma_{\text{stack}}^{\mathcal{F}}(r)]. \end{aligned} \quad (19)$$

In addition, galaxy clustering will also contribute to the stacked profile, primarily on large scales. We model clustering with the halo model framework (Cooray & Sheth 2002), where large-scale clustering is described by the correlation within (one-halo) and between (two-halo) dark matter halos. $\Sigma_{\text{stack}}^{1\text{h}}$ and $\Sigma_{\text{stack}}^{2\text{h}}$ represent the profile for one- and two-halo clustering, respectively.

In practice, there is no well-defined boundary between the stellar halo of a galaxy and unbound stars in the dark matter halo, and the definition of IHL (or ICL) varies in the literature. To some degree, the galaxy extension term and the one-halo term each partially comprise stars not bound to individual galaxies in the halo. Since there are different definitions of IHL (or ICL) and the one-halo term in the literature, here we describe how our modelled components are defined.

In our definition, the galaxy extension describes emission associated with each galaxy, whereas the one-halo term accounts for other galaxies, their extensions, and diffuse stars in the same halo, as illustrated in Fig. 10. When we stack on a central galaxy, the galaxy extension term accounts for the extended emission around the stacked galaxy, and the one-halo term describes diffuse stars, undetected galaxies, and extension around all the satellite galaxies beyond masking limit in the same halo. Whereas, when we stack on a satellite galaxy, the galaxy extension term only includes the extended halo around that satellite galaxy, and all the other components are described by the one-halo term. In our sample, we estimate that $\sim 60\%$ of stacked galaxies are central galaxies, and $\sim 40\%$ are satellite galaxies (See Table 2).

9.3. Modeling the Stacked Galaxy Profile

The stacked galaxy profile $\Sigma_{\text{stack}}^{\text{gal}}(r) = \Sigma^{\text{gal}}(r) \otimes PSF_{\text{stack}}(r)$, is the intrinsic galaxy profile Σ^{gal} , including the galaxy shape and the extended stellar halo, convolved with PSF_{stack} . Following Wang et al. (2019), we model Σ^{gal} with a double Sersic function:

$$\begin{aligned} \Sigma^{\text{gal}}(r) &= A^{\text{gal}} \left(10^{I_{e,1}} \exp \left\{ -b_{n1} \left[(r/R_{e,1})^{1/n_1} - 1 \right] \right\} \right. \\ &\quad \left. + 10^{I_{e,2}} \exp \left\{ -b_{n2} \left[(r/(R_{e,1} + R_{e,2}))^{1/n_2} - 1 \right] \right\} \right). \end{aligned} \quad (20)$$

Wang et al. (2019) performed a stacking analysis on isolated galaxies from Hyper Suprime-Cam (HSC) images, and fitted the stacked profile of their high-concentration samples with this model. The first term captures the galaxy shape, and the second term models the extended emission. Due to the lack of angular resolution in CIBER data, we are sensitive to the extended profile, and therefore we only vary $R_{e,2}$ to fit our stacked profile. We fix all of the other parameters to the best fit

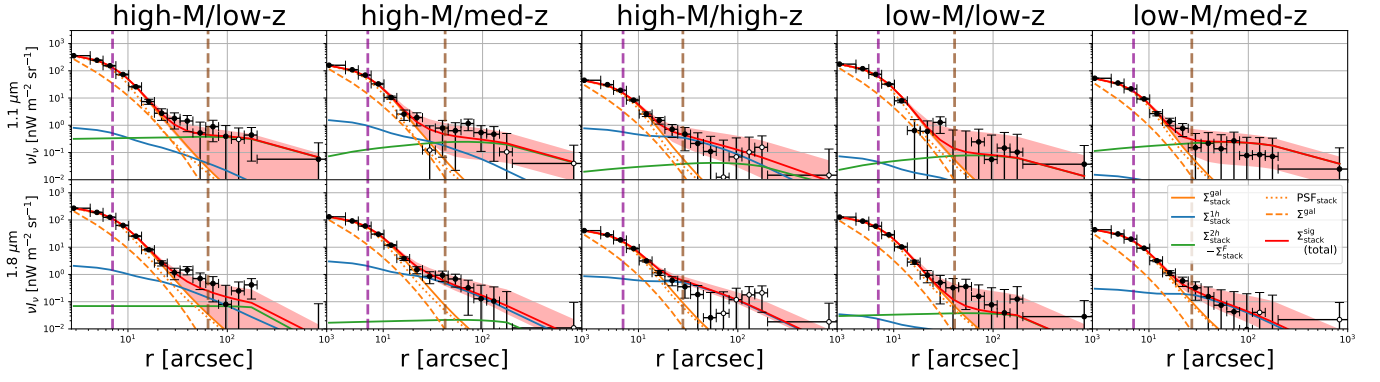


Figure 8. The stacked profile (black data) of each sub-sample stack averaged over five CIBER fields in the $1.1 \mu\text{m}$ (top) and $1.8 \mu\text{m}$ (bottom) bands. Red lines and shaded regions indicate the median and 68% confidence interval of the joint fit constrained through MCMC, respectively. The blue, green, and orange solid lines show the best-fit model of the stacked one-halo, two-halo, and galaxy profile term from MCMC. The orange dashed and dotted lines show the best-fit intrinsic galaxy profile Σ^{gal} and the PSF_{stack} model. The purple and brown dashed lines mark the pixel size ($7''$) and R_{200} value inferred from MICECAT. Open circles represent negative data points.

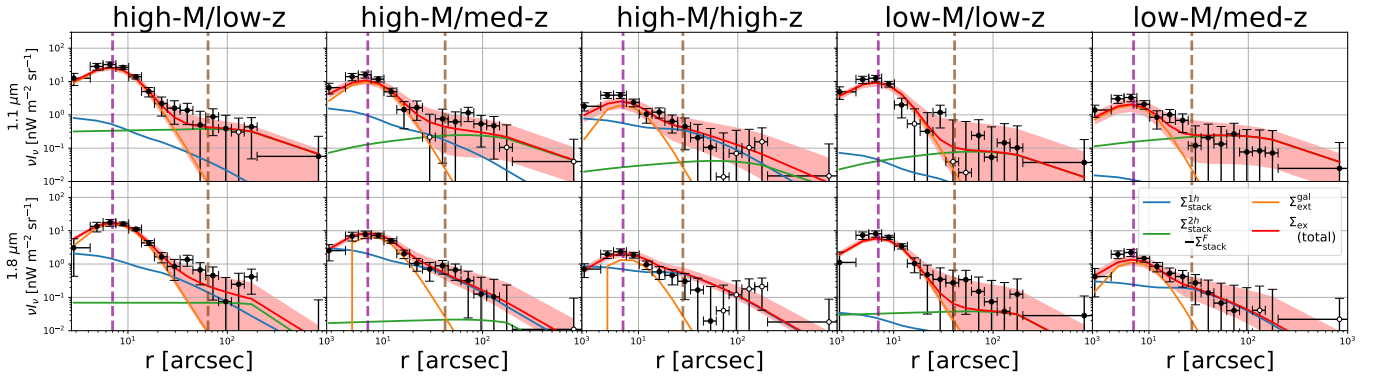


Figure 9. The measured (black data) and modeled (red) excess profile Σ_{ex} (black data) of each case shown in Fig. 8. Note the excess profile is defined by the difference of the stacked profile and PSF_{stacked} model (orange dotted line). other lines are same as the ones shown in Fig. 8.

939 values given by Table 3 of Wang et al. (2019), although 933
940 when convolved, the total closely follows the PSF⁹. 934

941 Our one- and two-halo clustering models, $\Sigma_{\text{stack}}^{1\text{h}}$ and 945
942 $\Sigma_{\text{stack}}^{2\text{h}}$, and the filtered signal $\Sigma_{\text{stack}}^{\mathcal{F}}$, are constructed 950
943 from the MICECAT simulation. MICECAT includes 947
944 central and satellite galaxies of each halo, and each 948
945 galaxy has a halo ID, enabling us to decouple the one- 949
946 halo and two-halo contribution in the stacked signal, and 950
947 thus to take into account the complication that we have 951
948 both central and satellite galaxies in our samples. We 952
949 model the one-halo term $\Sigma_{\text{stack}}^{1\text{h}}$ from MICECAT using 953
950 the following steps:

- 951 1. Select the stacked target in the catalog using the 954
952 same selection criteria. 955

- 953 2. For each target galaxy, generate a source map (us- 954
955 ing PSF_{instr} for all galaxies residing in the same 956
957 halo except for the target galaxy. 958
- 959 3. Generate a source mask using the same prescrip- 960
961 tion as our data. 962
- 963 4. Stack on the target source position. 964
- 965 5. Iterate steps (2)-(4) for all target sources. 966

960 The derived stacked profile provides our template for 961
962 the one-halo term, $T_{\text{stack}}^{1\text{h}}$. The filtered signal term $\Sigma_{\text{stack}}^{\mathcal{F}}$ 963
964 accounts for the loss of clustering signal from filtering. 965
966 $\Sigma_{\text{stack}}^{\mathcal{F}}$ is the stacked profile on the 2-D polynomial fil- 967
968 tered map (the second term of Eq. 13), which can be 969
970 modeled by filtering the simulated map from MICECAT. 971
972 We model the two-halo term $\Sigma_{\text{stack}}^{2\text{h}} - \Sigma_{\text{stack}}^{\mathcal{F}}$ after filtering 973
974 with the following process:

- 969 1. Make a CIBER-sized mock image from all the cat- 970
971 alog sources with the model PSF_{instr} , and mask 972

⁹ In Wang et al. (2019), the values of $R_{e,1}$ and $R_{e,2}$ are reported 957
958 in terms of $x_{e,1} = R_{e,1}/R_{200}$ and $x_{e,2} = R_{e,2}/R_{200}$. R_{200} is the 959
960 projected virial radius of the host dark matter halo in angular 961
962 units, and its value for each sub-samples is given in Table 2. 963

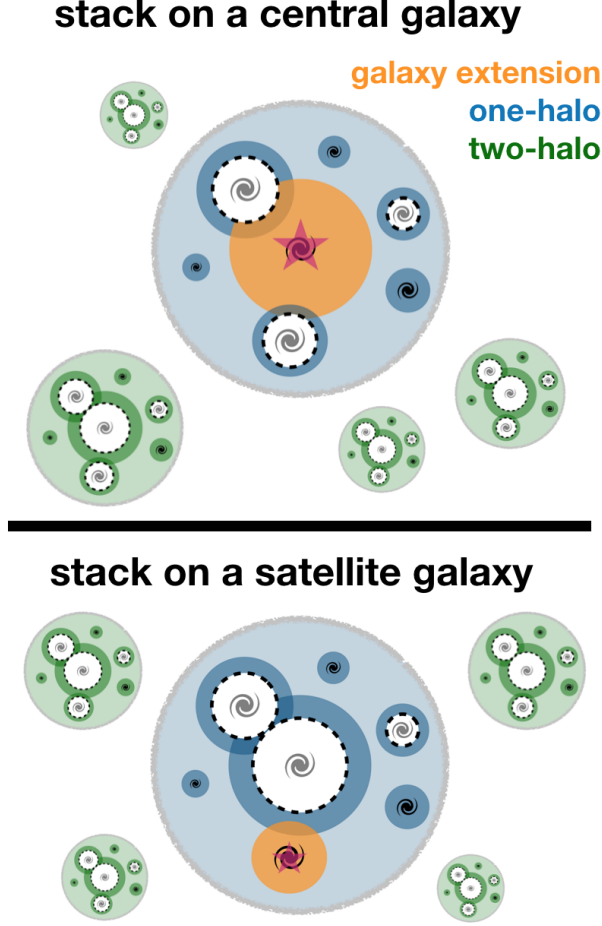


Figure 10. Illustration of the components in our model when stacking on a central (top) or a satellite (bottom) galaxy. The dark regions show the galaxy extensions associated with each galaxy, and the light blue and green regions show diffuse stars in the halos that are not tightly bound to any galaxy. The white parts with black dashed boundaries show the masked regions. The smaller galaxies without masks are fainter than the masking cutoff. The magenta stars and the orange regions show the stacked galaxy and its extension. The blue regions represent the one-halo term, and the green regions show the two-halo term contributed by emission from other halos. When stacking on a central galaxy, the one-halo term includes the satellite galaxy extensions beyond the masking radius, as well as faint satellite galaxies and their stellar halos. When stacking on a satellite galaxy, the one-halo term includes the extensions of both the central and the satellite galaxies beyond their masks, as well as the fainter satellite galaxies.

970 it with a source mask generated using the same
971 masking process applied to the data.

972 2. Fit and subtract a 2-D polynomial map to the im-
973 age.

- 974 3. Select the stacked target in the catalog using the
975 same selection criteria as the real sources.
- 976 4. Perform stacking with the target source, subtract-
977 ing all galaxies within the same halo to remove the
978 target galaxy and the one-halo contribution.
- 979 5. Iterate on step (4) to derive a stacked profile of
980 the filtered two-halo signal.

981 The resulting stacked profile, $T_{\text{stack}}^{2\text{h}-\mathcal{F}}$, is a model for
982 $\Sigma_{\text{stack}}^{2\text{h}} - \Sigma_{\text{stack}}^{\mathcal{F}}$, which provides our template for the two-
983 halo term. This process was performed on 400 realiza-
984 tions with CIBER-sized mock images from MICECAT,
985 and we take the average stacked profile as the one-halo
986 and filtered two-halo templates. As diffuse stars and
987 faint galaxies below the resolution limit of MICECAT
988 will not be accounted for, we assign free amplitudes to
989 the one-halo and two-halo templates, which are then
990 fit to the observed stacked data. Therefore, our three-
991 parameter $(R_{e,2}, A_{1\text{h}}, A_{2\text{h}})$ model can be written as

$$\begin{aligned} \Sigma_{\text{stack}}(r, \{R_{e,2}, A_{1\text{h}}, A_{2\text{h}}\}) \\ = \Sigma^{\text{gal}}(r, \{R_{e,2}\}) \otimes \text{PSF}_{\text{stack}}(r) \\ + A_{1\text{h}} T_{\text{stack}}^{1\text{h}}(r) + A_{2\text{h}} T_{\text{stack}}^{2\text{h}-\mathcal{F}}(r). \end{aligned} \quad (21)$$

992 We note that the one- and two-halo profiles already in-
993 clude the PSF convolution in our model.

994 9.4. Model Fitting

995 For each CIBER field and band, we fit the ex-
996 cess profile Eq. 6, to a three-parameter model
997 $\Sigma_{\text{ex}}^{\text{m}}(r, \{R_{e,2}, A_{1\text{h}}, A_{2\text{h}}\})$ (Eq. 21) using a Markov Chain
998 Monte Carlo (MCMC). We assume a Gaussian likeli-
999 hood, which is given by

$$\begin{aligned} \chi^2 &= (\Sigma_{\text{ex}}^{\text{d}} - \Sigma_{\text{ex}}^{\text{m}})^T C_{\text{ex}}^{-1} (\Sigma_{\text{ex}}^{\text{d}} - \Sigma_{\text{ex}}^{\text{m}}) \\ \ln \mathcal{L} &= -\frac{1}{2} \chi^2 - \frac{1}{2} \ln |C_{\text{ex}}| + \text{constant}, \end{aligned} \quad (22)$$

1000 where the inverse covariance C_{ex}^{-1} is given by Eq. 9.

1001 We use the fit from individual fields for a consistency
1002 check. To provide a best estimate using the combination
1003 of all the fields that were observed at once, we also fit
1004 to the five CIBER fields using the joint likelihood:

$$\ln \mathcal{L} = \sum_{i=1}^{N_{\text{field}}} \ln \mathcal{L}_i \quad (23)$$

1005 where $N_{\text{field}} = 5$. Note that the PSF model is different
1006 for each field, so the information from different fields is
1007 combined in the likelihood.

1008 We use the affine-invariant MCMC sampler `emcee`
1009 (Foreman-Mackey et al. 2013) to sample from the pos-
1010 terior distribution. We set flat priors for $R_{e,2}$, $A_{1\text{h}}$, and

1011 A_{2h} in the range of $[10^{-4}R_{200}, R_{200}]$, $[0, 50]$, and $[0,$
 1012 $200]$, respectively. We use an ensemble of 100 walkers
 1013 taking 1000 steps with 150 burn-in steps. We checked
 1014 that the chains show good convergence by computing
 1015 the Gelman-Rubin statistic R (Gelman & Rubin 1992).
 1016 For all three parameters in all cases, we find $R < 1.1$.

10. RESULTS

1017 We show the MCMC results in Fig. 11 and Table 3,
 1018 for all cases listed in Table 2. As a sanity check, we cal-
 1019 culate the χ^2 value between the results from individual
 1020 fields and the joint fit using 100 data points for each of
 1021 the three parameters (5 fields \times 10 mag bins \times 2 bands).
 1022 The resulting χ^2 values indicate our fit is internally con-
 1023 sistent across the 5 CIBER fields. In Fig. 8 and Fig. 9,
 1024 we show the stacked and excess profile data averaged
 1025 over five fields, respectively, along with the marginal-
 1026 ized one-halo, two-halo, and galaxy profile model from
 1027 the joint fit. Fig. 12 shows the fitted intrinsic galaxy
 1028 profile Σ^{gal} (Eq. 20) and the one- and two- halo terms
 1029 in the ‘‘total’’ magnitude bin, also averaged over five
 1030 fields. The field-averaged profiles are only shown for vi-
 1031 sualization purposes; when we fit the data with MCMC,
 1032 the information is combined in the likelihood function
 1033 rather than in data space.

11. DISCUSSION

11.1. Missing Light in Galaxy Photometry

1034 Given the best-fitting extended galaxy profile, we
 1035 can calculate the fraction of flux missed in photomet-
 1036 ric galaxy surveys using a limited aperture. From our
 1037 model, the fraction of flux within a photometric aperture
 1038 can be approximated by $f_{\text{core}} \equiv L_{\text{core}}/(L_{\text{core}} + L_{\text{ext}})$,
 1039 where L_{core} and L_{ext} are the total flux in the core and ex-
 1040 tension profile (Eq. 19), respectively. In practice, there
 1041 are various ways to perform photometry. The Petrosian
 1042 flux (Petrosian 1976) is derived from aperture photom-
 1043 etry and thus it is the most straightforward method
 1044 to compare to our results. The Petrosian flux is de-
 1045 fined by the total flux within a multiplicative factor
 1046 of the Petrosian radius of sources. We obtain the Pet-
 1047 rosian radius and Petrosian flux from the SDSS catalog
 1048 of each stacked galaxy in our sample. In SDSS, the
 1049 Petrosian flux is calculated by integrating the emission
 1050 within twice the Petrosian radius¹⁰. With our galaxy
 1051 profile, we can calculate the fraction of flux within the
 1052 same radius (f_{petro}). The results are summarized in Ta-
 1053 ble 5.

1054 We also estimate the missing light fraction with the
 1055 ‘model magnitude’ given in SDSS (f_{model}). Rather than
 1056 integrating within a certain aperture size, the model
 1057 magnitude is derived by fitting the galaxy profile with an
 1058 exponential or de Vaucouleurs functional form, choos-
 1059 ing the one with the higher likelihood in the fitting¹¹.
 1060 While it is difficult to apply the same fitting procedure
 1061 to the sources in CIBER images, we can calculate the
 1062 ratio between the model flux and the Petrosian flux of
 1063 each source in the SDSS catalog, and thus infer the frac-
 1064 tion of missing light in the model flux. We find that
 1065 both the Petrosian flux, which measures source emis-
 1066 sion within a limited aperture size, and the model flux
 1067 derived from fitting a light profile to the small-radii re-
 1068 gions of the galaxy, miss $\sim 20\%$ of the total galaxy
 1069 light, a deficit detected at $\sim 7\sigma$ ($\sim 4\sigma$) level for Pet-
 1070 rosian (model) flux when combing constraints from all
 1071 five sub-samples. This value is slightly larger than the
 1072 light fraction in our galaxy extension term (~ 10 to 20
 1073 %). Our results on the missing light fraction in the
 1074 Petrosian flux is in agreement with previous analytical
 1075 calculation (Graham et al. 2005). Interestingly, Tal &
 1076 van Dokkum (2011) probed the radial profile of $z \sim 0.34$
 1077 luminous red galaxies (LRGs) in SDSS with a stacking
 1078 analysis, and they also found $\sim 20\%$ of the total light
 1079 missing at large radii when fitting a Sersic model to in-
 1080 dividual galaxies. Although their galaxy samples are
 1081 at somewhat higher mass ($M_* \sim 10^{11} - 10^{12} M_{\odot}$), and
 1082 model magnitudes are fitted with a different functional
 1083 form, we arrive at a similar fraction of missing flux.

11.2. Extended Stellar Halo

1084 The Illustris simulation (Rodríguez-Gomez et al.
 1085 2016) traces the dynamics and merger history of stellar
 1086 particles and estimates the ‘‘ex-situ’’ population of stars
 1087 that formed in other galaxies, and were later stripped
 1088 and accreted into a new galaxy. The shaded region in the
 1089 left panel of Fig. 13 shows the ex-situ stellar mass frac-
 1090 tion at $z = 0$ from the Illustris simulation (Rodríguez-
 1091 Gomez et al. 2016). Although it is difficult to mea-
 1092 sure the ex-situ component in observations, Huang et al.
 1093 (2018) has studied individual stellar halos out to 100 kpc
 1094 in more massive galaxies ($10^{11} M_{\odot} \lesssim M_* \lesssim 10^{12} M_{\odot}$)
 1095 at higher redshifts ($z \sim 0.4$) in HSC images, find-
 1096 ing that the fraction of stellar mass between 10 and
 1097 100 kpc is in good agreement with the ex-situ frac-
 1098 tion constraints from Illustris (Rodríguez-Gomez et al.
 1099 2016). In addition, Wang et al. (2019) probe the stel-
 1100 lar halo around local ($0 \lesssim z \lesssim 0.25$) low-mass galaxies

¹⁰ https://www.sdss.org/dr12/algorithms/magnitudes/#mag_petro

¹¹ See <https://www.sdss.org/dr12/algorithms/magnitudes/> for the detailed descriptions on model magnitude.

Table 3. Summary of parameter constraints from the joint fit in each case listed in Table 2. For the cases with less than a 2σ detection (95% confidence interval), we quote the 2σ upper bound. For detections, the $+/-$ values enclose the 68% confidence interval.

Name	1.1 μm	1.1 μm	1.1 μm	1.8 μm	1.8 μm	1.8 μm
	$R_{e,2}$ [arcsec]	A_{1h}	A_{2h}	$R_{e,2}$ [arcsec]	A_{1h}	A_{2h}
mag bin #1	< 2.76	< 6.06	< 48.91	< 2.53	< 5.72	< 58.05
mag bin #2	$2.25^{+0.14}_{-0.23}$	< 4.70	< 24.22	$1.94^{+0.12}_{-0.16}$	< 3.44	< 24.76
mag bin #3	$1.85^{+0.17}_{-0.28}$	< 4.18	< 18.94	$1.94^{+0.16}_{-0.16}$	< 2.96	< 18.30
mag bin #4	$1.85^{+0.25}_{-0.21}$	< 1.16	< 6.87	$1.63^{+0.21}_{-0.14}$	$0.77^{+0.23}_{-0.23}$	< 6.59
total	$1.98^{+0.17}_{-0.17}$	< 1.41*	< 7.30	$1.85^{+0.08}_{-0.15}$	$1.01^{+0.24}_{-0.24}$	< 6.86
high-M/low-z	$2.30^{+0.16}_{-0.29}$	< 4.76	< 25.58	$2.17^{+0.18}_{-0.18}$	< 4.2	< 33.10
high-M/med-z	$2.27^{+0.37}_{-0.32}$	< 6.42	< 19.53	$2.22^{+0.19}_{-0.28}$	$3.37^{+1.99}_{-1.17}$	< 22.76
high-M/high-z	$1.98^{+0.30}_{-0.44}$	< 1.88	< 9.08	$1.85^{+0.26}_{-0.22}$	$1.39^{+0.43}_{-0.35}$	< 6.19
low-M/low-z	$1.98^{+0.18}_{-0.30}$	< 3.18	< 16.38	$1.89^{+0.21}_{-0.17}$	< 2.77	< 17.65
low-M/med-z	$1.67^{+0.29}_{-0.36}$	< 1.30	< 11.30	$1.50^{+0.21}_{-0.24}$	< 1.01	< 7.58

NOTE—In 1.1 μm “total” bin, the 68% confidence interval of one-halo amplitude A_{1h} is $0.54^{+0.42}_{-0.38}$, approximately an 1σ detection.

Table 5. Fraction of flux in core component compared to flux captured in Petrosian and SDSS model flux, assuming the galaxy light profile follows the stacking results in this work. The total row shows the weighted average of the five listed sub-samples.

Name	1.1 μm	1.1 μm	1.1 μm	1.8 μm	1.8 μm	1.8 μm
	f_{core}	f_{petro}	f_{model}	f_{core}	f_{petro}	f_{model}
high-M/low-z	$0.79^{+0.04}_{-0.02}$	$0.78^{+0.08}_{-0.10}$	$0.84^{+0.11}_{-0.12}$	$0.81^{+0.02}_{-0.02}$	$0.80^{+0.07}_{-0.10}$	$0.85^{+0.10}_{-0.12}$
high-M/med-z	$0.81^{+0.04}_{-0.05}$	$0.74^{+0.07}_{-0.13}$	$0.78^{+0.08}_{-0.15}$	$0.83^{+0.04}_{-0.03}$	$0.75^{+0.08}_{-0.11}$	$0.78^{+0.10}_{-0.13}$
high-M/high-z	$0.86^{+0.06}_{-0.04}$	$0.73^{+0.07}_{-0.16}$	$0.77^{+0.15}_{-0.19}$	$0.89^{+0.03}_{-0.04}$	$0.75^{+0.07}_{-0.16}$	$0.79^{+0.16}_{-0.18}$
low-M/low-z	$0.84^{+0.04}_{-0.02}$	$0.78^{+0.05}_{-0.11}$	$0.80^{+0.10}_{-0.12}$	$0.85^{+0.02}_{-0.03}$	$0.79^{+0.05}_{-0.11}$	$0.81^{+0.10}_{-0.12}$
low-M/med-z	$0.89^{+0.04}_{-0.04}$	$0.78^{+0.06}_{-0.16}$	$0.80^{+0.09}_{-0.16}$	$0.92^{+0.03}_{-0.03}$	$0.80^{+0.06}_{-0.15}$	$0.83^{+0.10}_{-0.14}$
total	$0.83^{+0.02}_{-0.01}$	$0.77^{+0.03}_{-0.06}$	$0.80^{+0.05}_{-0.06}$	$0.86^{+0.01}_{-0.01}$	$0.78^{+0.03}_{-0.05}$	$0.81^{+0.05}_{-0.06}$

1105 ($9.2 M_{\odot} < \log M_{*} < 11.4 M_{\odot}$) with a stacking analysis
 1106 on HSC images in r -band. They stacked galaxies out to
 1107 ~ 120 kpc within several stellar mass bins. For each bin,
 1108 they split the sources into low and high concentration
 1109 populations, defined by $C < 2.6$ and $C > 2.6$, where
 1110 $C = R_{90}/R_{50}$ is the ratio of the radii that contain 90%
 1111 and 50% of the r -band Petrosian flux.

1112 CIBER extends the HSC measurements to higher red-
 1113 shifts and longer wavelength bands. Armed with light
 1114 profile fits, we can quantify the luminosity fraction in
 1115 the extended stellar halo around the stacked sources.
 1116 The left panel of Fig. 13 shows the fraction of stel-
 1117 lar flux between radii of 10 and 100 kpc, using the fit-
 1118 ted galaxy profile from CIBER and HSC (Wang et al.
 1119 2019). We observe that $\sim 50\%$ of the flux originates at

1120 galactocentric distances between 10 and 100 kpc. Wang
 1121 et al. (2019) re-scaled their images to physical units be-
 1122 fore stacking, whereas in our analysis we stack sources
 1123 in observed angular units. Therefore, the variations in
 1124 our measurements are mostly due to the variation of the
 1125 conversion factor from angular to physical units for each
 1126 galaxy in our stack. Our constraints are consistent with
 1127 the HSC results in the highest mass bin.

1128 Both CIBER and HSC are consistent with the ex-situ
 1129 fraction from Illustris at $z = 0$, but are systematically
 1130 higher than the median value from Illustris (the grey
 1131 line in Fig. 13). One possible explanation is that the
 1132 flux between 10 and 100 kpc is not a perfect proxy of
 1133 the ex-situ population for lower mass galaxies. For ex-
 1134 ample, D’Souza et al. (2014) has shown that the transi-

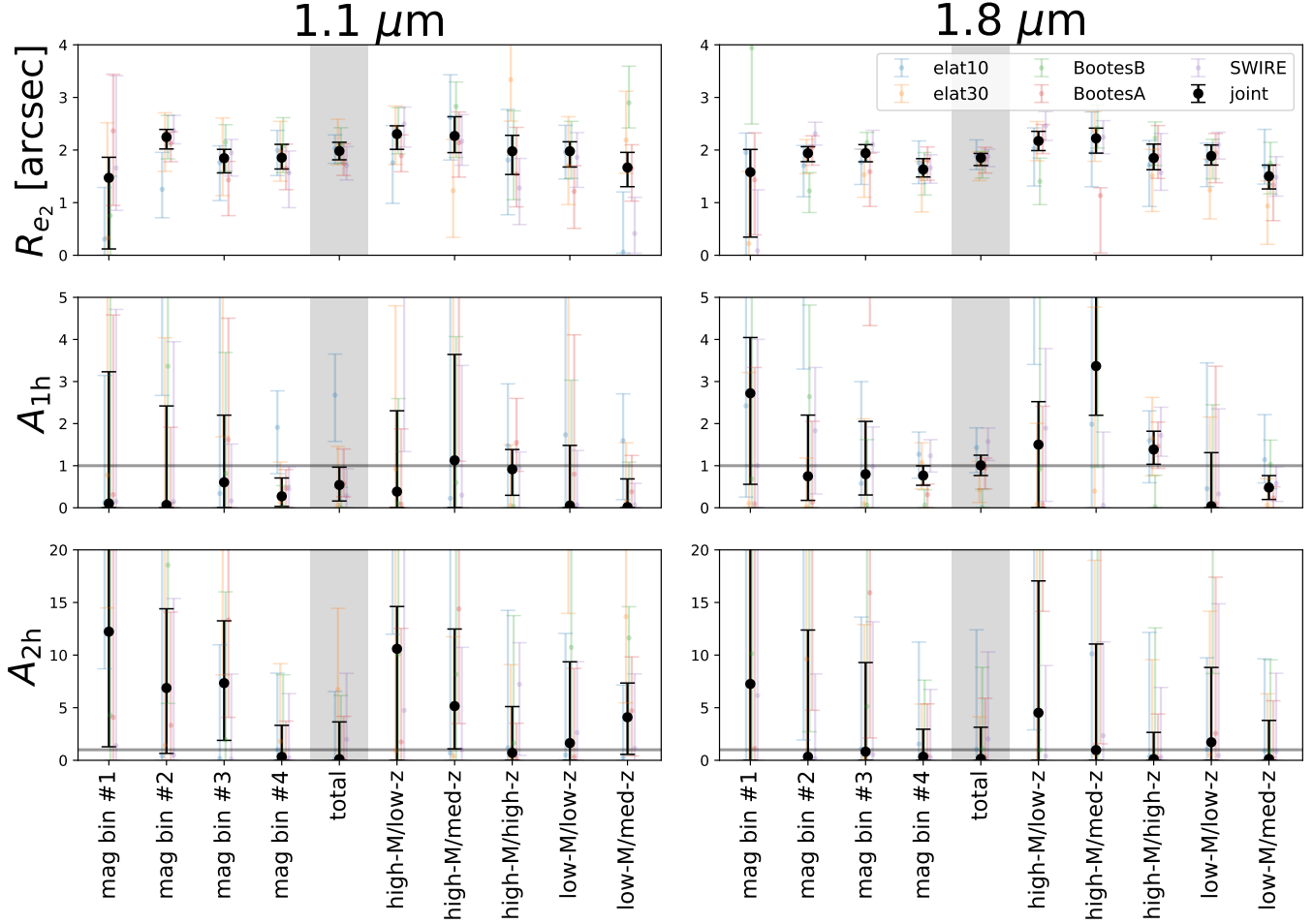


Figure 11. Marginalized parameter constraints from MCMC for each case listed in Table 2. The data points and error bars are the median and 68% confidence intervals from MCMC. Black data points show the joint fit from all five fields, with colored points for the individual fields. The gray horizontal lines in the middle and bottom panels mark $A_{1h} = 1$ and $A_{2h} = 1$, which are the clustering amplitudes given by MICECAT. The shaded regions show the total stack over all $17 < m_{1.1} < 20$ galaxies.

1135 tion scale between in-situ and ex-situ components varies 1152
 1136 across a wide range from ~ 10 to ~ 50 kpc, depending 1153
 1137 on the stellar mass and concentration of the galaxies.
 1138 Nevertheless, given the limited information in stacking, 1154
 1139 we use this definition to associate the luminosity from 1155
 1140 beyond 10 kpc with IHL. 1156

1141 In addition, we also show the fraction of flux with 20 1157
 1142 kpc radius cut in the right panel of Fig. 13. We find that 1158
 1143 $\sim 25\%$ of galaxy fluxes are from outside 20 kpc. The 1159
 1144 CIBER constraints shown in Fig. 13 are summarized in 1160
 1145 table 5. 1161

1146 With the galaxy profile from CIBER and HSC, we 1162
 1147 can estimate the EBL contribution from the extended 1163
 1148 regions at the redshift of our stacked sources. We model 1164
 1149 this quantity in the following steps: 1165

- 1150 1. For any given radius cut r_{cut} , we model the frac- 1166
 1151 tion of light beyond r_{cut} as a function of stellar 1167

mass by fitting a line to all CIBER and HSC data 1152
 points in logarithmic space. 1153

2. We estimate total stellar mass density by integrat- 1154
 ing the stellar mass function from Muzzin et al. 1155
 (2013) (we take their single Schechter function fit 1156
 with all samples in $0.2 \leq z < 0.5$ bin, approxi- 1157
 mately the redshift of our sources). 1158
3. For each r_{cut} , we apply the fraction derived in step 1159
 1 to the stellar mass function, and integrate to get 1160
 the stellar mass density from sources outside r_{cut} . 1161
4. Assuming the mass-to-light ratio is the same for 1162
 all galaxies, the ratio between step 3 and step 2 1163
 is our estimate of the EBL fraction from extended 1164
 sources as a function of r_{cut} . 1165

The results are shown in Fig. 14. We get approximately 1166
 50/30 % of extended emission in the EBL with $r_{\text{cut}} =$ 1167

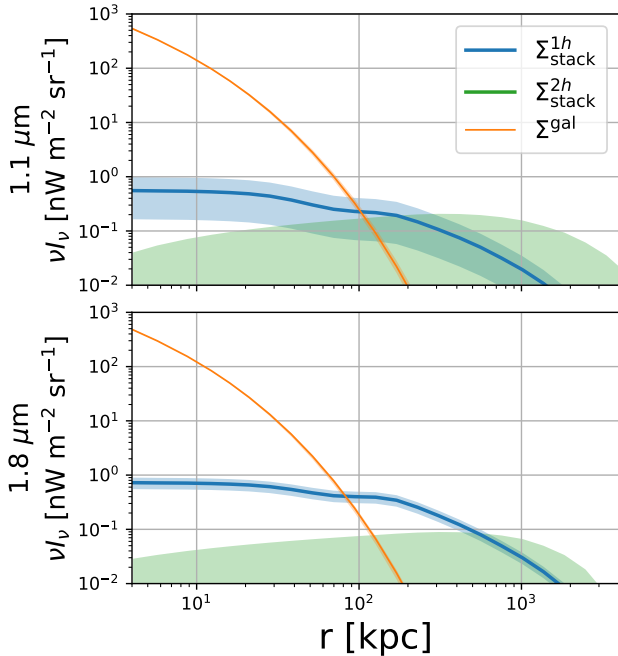


Figure 12. The fitted intrinsic galaxy profile Σ_{gal} (Eq. 20) (orange), stacked one-halo (blue) and two-halo (green) profiles in the “total” magnitude bin averaged over five CIBER fields in the $1.1 \mu\text{m}$ (top) and $1.8 \mu\text{m}$ (bottom) bands. We convert the angular scale to physical units (kpc) using the median conversion factor inferred from MICECAT (Table 2). Solid lines and shaded regions indicate the median and 68% confidence interval of the joint fit constrained through MCMC, respectively.

1188 where $\sum_{m_{1.1} < 20} L$ is the total light associate with bright
 1189 galaxies, and $\sum_{m_{1.1} < 20} L(> r_{\text{cut}})$ is the part of bright
 1190 galaxy emission beyond r_{cut} . $\sum_{\text{faint}} L$ represents the
 1191 light from faint galaxies as well as the unbound stars
 1192 in the halo, captured in the one-halo luminosity. Note
 1193 that we conservatively assume the one-halo luminosity
 1194 arises entirely from faint, gravitationally bound galax-
 1195 ies. However it is certainly true that some one-halo light
 1196 arises from unbound stars, as is readily observed in im-
 1197 ages of massive clusters at low redshift.

1198 From our stacking profile, the faint source emission
 1199 $\sum_{\text{faint}} L$ can be described by the total emission in the
 1200 one-halo term, L_{1h} ¹². For the bright sources, we define

$$\sum_{m_{1.1} < 20} L = L_{\text{gal}} \cdot N_{\text{eff}}, \quad (25)$$

1201 where L_{gal} is the total light in the galaxy profile term
 1202 from our stacking results, which describes the aver-
 1203 aged light of the galaxies within each stacking sample.
 1204 N_{eff} accounts for the fact that there are multiple bright
 1205 galaxies in the halo, and we infer the average N_{eff} value
 1206 from MICECAT. For our five stacking sub-samples, we
 1207 get $N_{\text{eff}} \sim 2$ to 5. From our fitted galaxy profile, we can
 1208 also calculate $L_{\text{gal}}(> r_{\text{cut}})$, and we apply the same N_{eff}
 1209 to model the extension from other bright galaxies:

$$\sum_{m_{1.1} < 20} L(> r_{\text{cut}}) = L_{\text{gal}}(> r_{\text{cut}}) \cdot N_{\text{eff}}. \quad (26)$$

1210 This results in

$$f_{\text{IHL}} = \frac{L_{\text{gal}}(> r_{\text{cut}})/L_{\text{gal}}}{1 + L_{1h}/(N_{\text{eff}} \cdot L_{\text{gal}})}. \quad (27)$$

1211 We show our constraints on f_{IHL} , as a function of halo
 1212 mass and redshift in Fig. 15 and 16, respectively. The
 1213 halo masses associated with our galaxies are inferred
 1214 from the MICECAT simulation, and using the SDSS
 1215 photometric redshifts. The CIBER data points shown
 1216 in Fig. 15 and 16 are summarized in Table 6.

1217 Note that the fraction of light beyond r_{cut} (the nu-
 1218 merator in Eq. 27) is shown in Fig. 13, where the higher
 1219 redshift bins have slightly higher values. However, in
 1220 Fig. 16, they have lower f_{IHL} . This is due to the increase
 1221 of the one-halo term with redshift. We show the ratio
 1222 of one-halo term and the stacked galaxy light in Fig. 17.
 1223 Note that this observable quantity tracks the evolution
 1224 of the one-halo luminosity, but lacks the N_{eff} term in
 1225 Eq. 27 derived from simulations. We compare with the

1168 10/20 kpc, respectively. Note that these values are close
 1169 to the fraction in the five individual stellar mass bins
 1170 from our stacking results. This is expected as our sam-
 1171 ples are at $\sim L^*$ scale, which are the representative pop-
 1172 ulation that contains the majority of the total stellar
 1173 emission of their redshift.

1174 11.3. Intra-halo Light Fraction

1175 The fraction of the total emission from a dark matter
 1176 halo associated with IHL, f_{IHL} , has been investigated
 1177 with both observation and theoretical modeling (e.g.,
 1178 Lin & Mohr 2004; Gonzalez et al. 2005; Purcell et al.
 1179 2007; D’Souza et al. 2014; Burke et al. 2015; Elias et al.
 1180 2018). With our stacking results, we can estimate the
 1181 total halo emission from the sum of the galaxy light
 1182 and one-halo terms. For the IHL, we consider the ex-
 1183 tended galaxy emission beyond $r_{\text{cut}} = 10/20$ kpc of all
 1184 the bright ($m_{1.1} < 20$) galaxies in the halo, noting that
 1185 $m_{1.1} = 20$ is also our choice of flux threshold for mask-
 1186 ing. Therefore, the IHL fraction f_{IHL} can be expressed
 1187 as

$$f_{\text{IHL}} = \frac{\sum_{m_{1.1} < 20} L(> r_{\text{cut}})}{\sum_{m_{1.1} < 20} L + \sum_{\text{faint}} L}, \quad (24)$$

¹² Our one-halo model also includes the outskirts of bright sources beyond the mask, but we checked that this component is negligible compared to the faint sources using the MICECAT simulation.

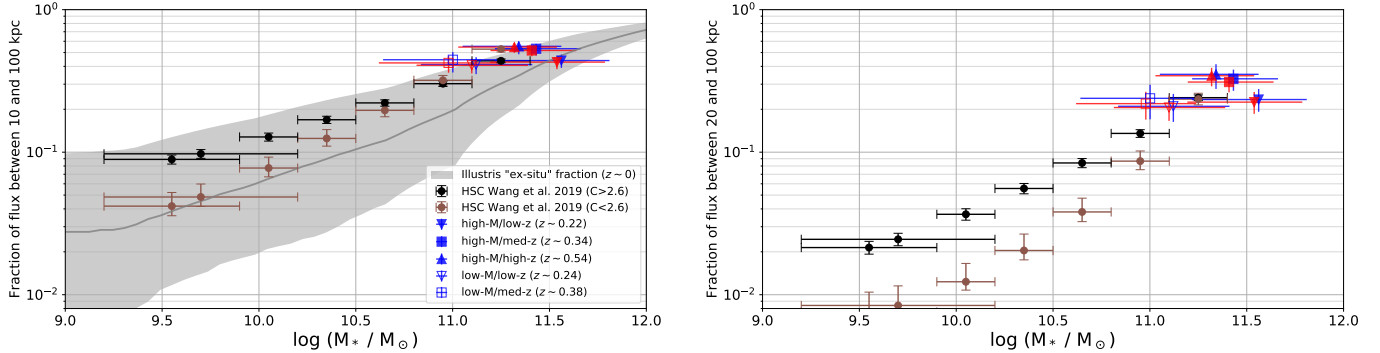


Figure 13. Fraction of flux between 10 (left)/20 (right) and 100 kpc from the galaxy profile derived from CIBER stacking (this work) in the 1.1 (blue) and 1.8 (red) μm bands and from HSC stacking (Wang et al. 2019). The HSC stacking is performed on low and high concentration populations ($C < 2.6$ and $C > 2.6$) at optical wavelengths (r band). The horizontal error bars define the lower and upper bounds of the stellar mass of each stacking sample. The grey line and the shaded regions in the left panel are the median, 16th, and 84th percentile of ex-situ stellar mass fraction at $z = 0$ from Illustris simulations (Rodriguez-Gomez et al. 2016). The shaded region shows the variance between individual galaxies in Illustris, whereas for CIBER and HSC, the error bars represent the standard error on the mean value.

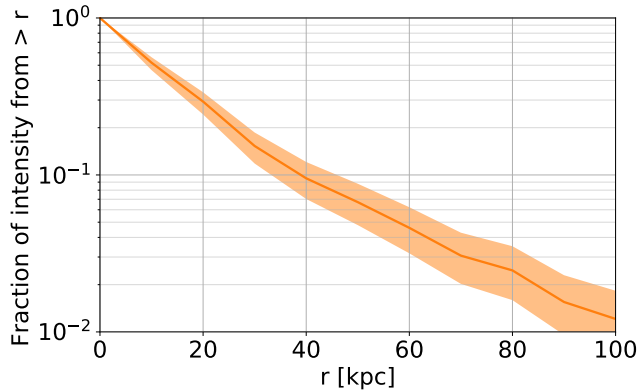


Figure 14. The fraction EBL intensity from galaxy extension as a function of r_{cut} . This is estimated with the light profile fits from CIBER (this work) and HSC Wang et al. (2019), and the stellar mass function from Muzzin et al. (2013).

1226 same quantity from the MICECAT simulation, where
 1227 the one-halo term includes all the unmasked faint galax-
 1228 ies and residual bright source emission outside the mask
 1229 due to the PSF. We detect a strong redshift evolution
 1230 of one-halo contribution compared with the MICECAT
 1231 simulation, which could be attributed to the unbound
 1232 stars that are not included in MICECAT.

1233 We compare our results with f_{IHL} from previous work,
 1234 including the Milky Way (Carollo et al. 2010), the An-
 1235 dromeda Galaxy (M31; Courteau et al. 2011), the ICL
 1236 fraction in individual galaxy groups and clusters (Gon-
 1237 zalez et al. 2005, 2007; Burke et al. 2015), and an analyt-
 1238 ical model (Purcell et al. 2007, 2008). Our results follow
 1239 a more gradual redshift evolution trend than reported
 1240 in massive clusters (Burke et al. 2015) (see Fig. 16).

1241 11.4. Color of the Galaxy Inner and Outer Regions

1242 We calculate the $m_{1.1} - m_{1.8}$ color of the inner and
 1243 outer region of the galaxy, defined by the total light
 1244 inside and outside 20 kpc physical scale in the fitted
 1245 galaxy profile. The results are summarized in Table 4.
 1246 Note the definition of inner and outer component here is
 1247 based on the intrinsic profile, which is different from the
 1248 core/extension separation using the stacked PSF defined
 1249 in Eq. 19. We have no detection of a color difference be-
 1250 tween the inner and outer regions in the two CIBER
 1251 bands. We also find similar inner and outer region color
 1252 with 10 kpc radius cut. Previous measurements in opti-
 1253 cal bands found that the galaxy outskirts are bluer
 1254 than their core (e.g., D’Souza et al. 2014; Huang et al.
 1255 2018). For comparison, we calculate the $m_{1.1} - m_{1.8}$
 1256 color of galaxy cores in MICECAT sources selected from
 1257 the same criteria, as well as from the empirical galaxy
 1258 model of Helgason et al. (2012) at $z = 0.3$, approxi-
 1259 mately the redshift of our samples. Our inner region
 1260 color is consistent with these models. To model the ex-
 1261 tension, we use a collection of elliptical galaxy spectra
 1262 from the population synthesis package GISSEL (Bruzual
 1263 A. & Charlot 1993) redshifted to $z = 0.3$. We also esti-
 1264 mate the extension color using an imaging study on the
 1265 local spiral galaxy NGC 5907 (Rudy et al. 1997). We
 1266 use their ratio of I band and J band flux in >1 arcmin
 1267 regions to approximate the $m_{1.1} - m_{1.8}$ extension color.
 1268 The rest-frame I and J band redshifted to $z \sim 0.3$ (ap-
 1269 proximately the redshift of our samples) are close to the
 1270 two CIBER bands. NGC 5907 shows a redder spectrum
 1271 than our galaxy extension, whereas the elliptical galaxy
 1272 spectrum template is slightly bluer than our samples. In
 1273 addition, the IHL constraints from Zemcov et al. (2014)

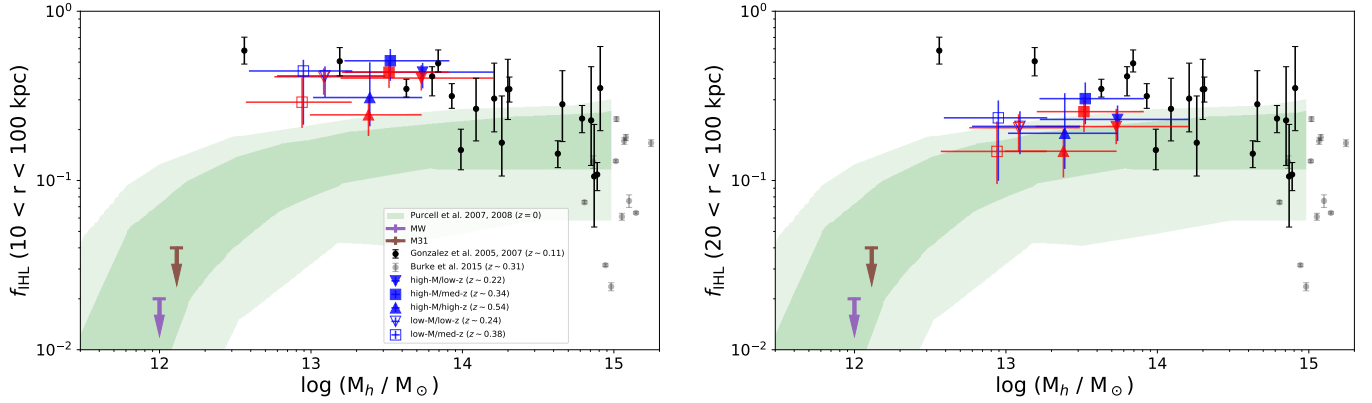


Figure 15. The IHL fraction f_{IHL} as a function of halo mass. The IHL is defined by the light beyond a radius r_{cut} around the galaxy. Here we consider three different r_{cut} values: 10 kpc (left) and 20 kpc (right). Blue and red data points show the constraints from this work in the 1.1 μm and 1.8 μm bands, respectively. Dark and light green shaded regions denote the 68% and 95% variations among galaxies from an analytical model at $z = 0$ (Purcell et al. 2007, 2008). The ICL fraction in individual galaxy groups and clusters from Gonzalez et al. (2005, 2007) and Burke et al. (2015) are shown in black and grey data points. The two downward arrows give upper limits for the Milky Way (Carollo et al. 2010) and Andromeda (M31) (Courteau et al. 2011).

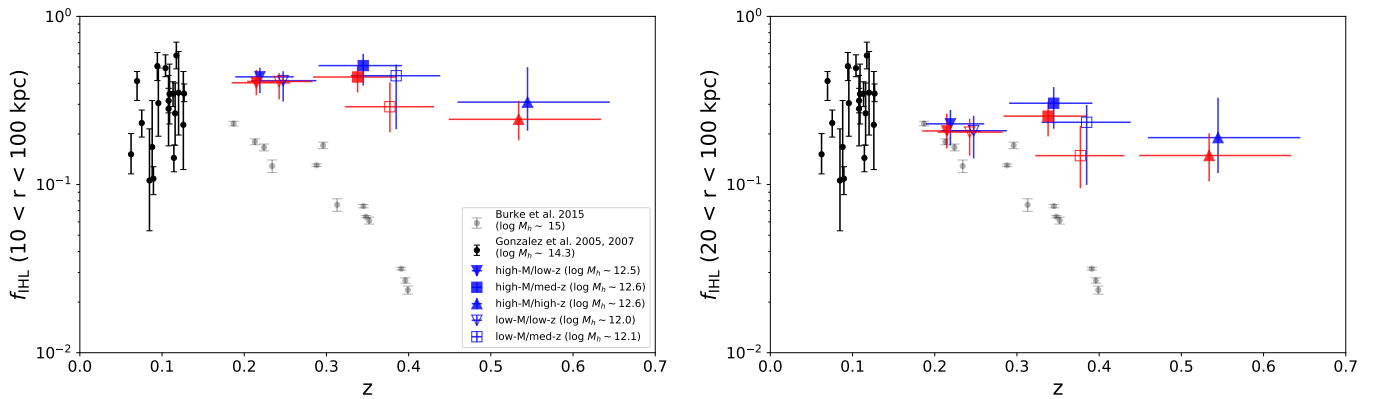


Figure 16. f_{IHL} constraints as in Fig. 15, but plotted as a function of redshift. The masses of the Burke et al. (2015) clusters are 100-1000 \times the halo masses associated with our galaxies.

1274 are also given in Table 4, but we note that Zemcov et al. 1290
 1275 (2014) reflects the integrated IHL from all redshifts. 1291 large-scale clustering signal is comparable to the current
 1292 uncertainties in the measurement.

11.5. One-halo and Two-halo Clustering

1276
 1277 The one-halo amplitude is detected in the 1.8 μm band
 1278 at the $\sim 4\sigma$ level in the “total” and “high-M/high-z”
 1279 cases, and at the $\sim 3\sigma$ level in “mag bin #4” and “high-
 1280 M/med-z” cases. One-halo clustering is not clearly de-
 1281 tected at the 1.1 μm band since the photocurrent from
 1282 sources is lower in this band. The one-halo amplitude
 1283 $A_{1\text{h}}$ is consistent with unity to within $\sim 2\sigma$, which im-
 1284 plies that our one-halo templates built from MICECAT
 1285 are sufficient to describe the clustering within halos of
 1286 our stacked samples. However, from our stacking re-
 1287 sults, it is unclear if this emission actually consists of
 1288 discrete galaxies as given in the MICECAT simulation.
 1289 Two-halo clustering is not detected in all cases since the

12. CONCLUSIONS

1293 By stacking galaxies from CIBER imaging data in
 1294 two near-infrared bands (1.1 and 1.8 μm), we detect ex-
 1295 tended emission in galaxies. The galaxies being stacked
 1296 ($\sim 30,000$ galaxies in total) are split into five sub-
 1297 samples from SDSS spanning redshifts $0.2 \lesssim z \lesssim 0.5$ and
 1298 stellar masses $10^{10.5} M_{\odot} \lesssim M_{*} \lesssim 10^{12} M_{\odot}$, comparable
 1299 to L_{*} galaxies at this redshift. We jointly fit a model
 1300 for the inherent galaxy light profile and large-scale one-
 1301 and two-halo clustering.

1302 With the galaxy profile, we estimate that $\sim 20\%$ of
 1303 total light is missing in galaxy photometry due to the
 1304 use of limited apertures, in agreement with previous es-
 1305 timates from the literature. We do not detect a 1.1-1.8

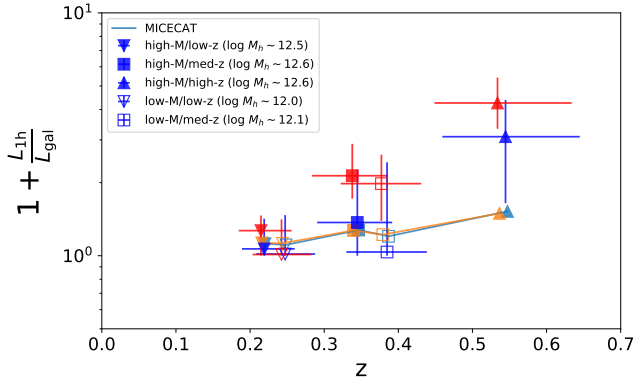


Figure 17. The ratio of the total one-halo term and stacked galaxy profile term from our stacking results (blue: $1.1 \mu\text{m}$, red: $1.8 \mu\text{m}$) compared with the MICECAT simulation (light blue: $1.1 \mu\text{m}$, orange: $1.8 \mu\text{m}$). We observe a somewhat stronger evolution, causing the fall-off of f_{IHL} with redshift seen in Fig. 16.

Table 4. Constraints on the color ($m_{1.1} - m_{1.8}$) of the galaxy inner and outer components. The $+/-$ values indicate 68% interval ranges. The total row shows the weighted average of five sub-samples. For comparison, we also show models of core color from MICECAT and an analytical prescription from Helgason et al. (2012) at $z = 0.3$. For the extension, we compare our results with spectra from a population synthesis code, GISSEL (Bruzual A. & Charlot 1993), and the outskirts of NGC 5907 redshifted to $z = 0.3$ (Rudy et al. 1997). The color of EBL fluctuations attributed to redshift-integrated IHL from Zemcov et al. (2014) is also shown.

Name	Inner	Outer
high-M/low-z	$0.42^{+0.20}_{-0.17}$	$0.36^{+0.34}_{-0.31}$
high-M/med-z	$0.54^{+0.25}_{-0.27}$	$0.46^{+0.24}_{-0.25}$
high-M/high-z	$0.65^{+0.31}_{-0.28}$	$0.61^{+0.31}_{-0.25}$
low-M/low-z	$0.39^{+0.20}_{-0.18}$	$0.37^{+0.41}_{-0.37}$
low-M/med-z	$0.56^{+0.23}_{-0.24}$	$0.44^{+0.50}_{-0.44}$
total	$0.49^{+0.10}_{-0.10}$	$0.47^{+0.14}_{-0.15}$
MICECAT	0.44 ± 0.07	
Helgason et al. (2012)	0.41	
GISSEL		0.32 ± 0.08
NGC 5907		1.41 ± 0.61
Zemcov et al. (2014)		$0.89^{+1.17}_{-1.08}$

nificance over the full sample of galaxies. These results suggest non-linear clustering could have a significant impact on modeling the IHL, but is not accounted for in previous fluctuation analysis by Zemcov et al. (2014). An IHL fluctuation model with one-halo clustering (e.g., Fernandez et al. 2010) is needed to fully account for the non-linear clustering in IHL modeling.

The intrinsic galaxy profile fitted from our stacking analysis suggests $\sim 50\%/25\%$ of the total galaxy light resides in the outskirts of galaxies at $r > 10/20$ kpc, respectively. This result is in agreement with previous HSC measurements at lower redshifts ($0 \lesssim z \lesssim 0.25$) and lower stellar masses ($10^{9.2} M_{\odot} < M_* < 10^{11.4} M_{\odot}$). The galaxy extension accounts for significant fraction of luminosity in L_* galaxies, but falls off below $M_* \sim 10^{11} M_{\odot}$. We measure a moderate increase in f_{IHL} with cosmic time, which we attribute to the decrease in one-halo contribution within the dark matter halo of our stacked samples. The previous fluctuation study using CIBER data (Zemcov et al. 2014) found that the IHL has comparable intensity to the IGL in the near-infrared EBL. While our study cannot constrain the whole IHL contribution to the EBL since we only study galaxies from a certain range of redshift and masses, our results suggest that $\sim L_*$ galaxy at $0.2 \lesssim z \lesssim 0.5$ have an extended light profile which contributes appreciable IHL to their host halos. As $\sim L_*$ galaxies are the representative population, which contain most of the IGL emission, the flux from the extension, and the one-halo term present in our galaxy samples, both need to be properly accounted for in future EBL photometry and fluctuation measurements.

μm color difference in the inner and outer region of our galaxy samples.

While we do not detect two-halo clustering, we detect one-halo clustering in the $1.8 \mu\text{m}$ band at $4\text{-}\sigma$ sig-

ACKNOWLEDGMENTS

We would like to thank the anonymous referee for valuable comments that improved the manuscript. We thank the dedicated efforts of the sounding rocket staff at NASA Wallops Flight Facility and White Sands Missile Range. This work was supported by NASA APRA research grants NNX07AI54G, NNG05WC18G, NNX07AG43G, NNX07AJ24G, NNX10AE12G, and 80NSSC20K0595. Initial support was provided by an award to J.B. from the Jet Propulsion Laboratory's Director's Research and Development Fund. Japanese participation in CIBER was supported by KAKENHI (20.34, 18204018, 19540250, 21340047, 21111004, 24111717, 26800112, and 15H05744) from Japan Society for the Promotion of Science (JSPS) and the Ministry of Education, Culture, Sports, Science and Technology (MEXT). Korean participation in CIBER was supported by the Pioneer Project from Korea Astronomy and Space Science Institute (KASI). Y.-T. C. acknowledges support by the Ministry of Education, Taiwan through the Taiwan-Caltech Scholarship. C. H. N. acknowledges support by NASA Headquarters under the NASA Earth and Space Science Fellowship Program - Grant 80NSSCK0706. Part of the research was carried out at the Jet Propulsion Laboratory, California Institute of Technology, under a contract with the National Aeronautics and Space Administration (80NM0018D0004).

This publication makes use of data products from the Two Micron All Sky Survey, which is a joint project of the University of Massachusetts and the Infrared Processing and Analysis Center/California Institute of Technology, funded by the National Aeronautics and Space Administration and the National Science Foundation.

The Pan-STARRS1 Surveys (PS1) and the PS1 public science archive have been made possible through contributions by the Institute for Astronomy, the University of Hawaii, the Pan-STARRS Project Office, the Max-Planck Society and its participating institutes, the Max Planck Institute for Astronomy, Heidelberg and the Max Planck Institute for Extraterrestrial Physics, Garching, The Johns Hopkins University, Durham University, the University of Edinburgh, the Queen's University Belfast, the Harvard-Smithsonian Center for Astrophysics, the Las Cumbres Observatory Global Telescope Network Incorporated, the National Central University of Taiwan, the Space Telescope Science Institute, the National Aeronautics and Space Administration under Grant No. NNX08AR22G issued through the Planetary Science Division of the NASA Science Mission Directorate, the

National Science Foundation Grant No. AST-1238877, the University of Maryland, Eotvos Lorand University (ELTE), the Los Alamos National Laboratory, and the Gordon and Betty Moore Foundation.

Funding for the Sloan Digital Sky Survey IV has been provided by the Alfred P. Sloan Foundation, the U.S. Department of Energy Office of Science, and the Participating Institutions. SDSS-IV acknowledges support and resources from the Center for High-Performance Computing at the University of Utah. The SDSS web site is www.sdss.org.

SDSS-IV is managed by the Astrophysical Research Consortium for the Participating Institutions of the SDSS Collaboration including the Brazilian Participation Group, the Carnegie Institution for Science, Carnegie Mellon University, the Chilean Participation Group, the French Participation Group, Harvard-Smithsonian Center for Astrophysics, Instituto de Astrofísica de Canarias, The Johns Hopkins University, Kavli Institute for the Physics and Mathematics of the Universe (IPMU) / University of Tokyo, the Korean Participation Group, Lawrence Berkeley National Laboratory, Leibniz Institut für Astrophysik Potsdam (AIP), Max-Planck-Institut für Astronomie (MPIA Heidelberg), Max-Planck-Institut für Astrophysik (MPA Garching), Max-Planck-Institut für Extraterrestrische Physik (MPE), National Astronomical Observatories of China, New Mexico State University, New York University, University of Notre Dame, Observatório Nacional / MCTI, The Ohio State University, Pennsylvania State University, Shanghai Astronomical Observatory, United Kingdom Participation Group, Universidad Nacional Autónoma de México, University of Arizona, University of Colorado Boulder, University of Oxford, University of Portsmouth, University of Utah, University of Virginia, University of Washington, University of Wisconsin, Vanderbilt University, and Yale University.

This work has made use of data from the European Space Agency (ESA) mission *Gaia* (<https://www.cosmos.esa.int/gaia>), processed by the *Gaia* Data Processing and Analysis Consortium (DPAC, <https://www.cosmos.esa.int/web/gaia/dpac/consortium>). Funding for the DPAC has been provided by national institutions, in particular the institutions participating in the *Gaia* Multilateral Agreement.

This work has made use of CosmoHub. CosmoHub has been developed by the Port d'Informació Científica (PIC), maintained through a collaboration of the Institut de Física d'Altes Energies (IFAE) and the Centro de Investigaciones Energéticas, Medioambientales y Tecnológicas (CIEMAT) and the Institute of Space Sciences (CSIC & IEEC), and was partially funded by the

1417 "Plan Estatal de Investigación Científica y Técnica y de
1418 Innovación" program of the Spanish government.

1419 *Software:* astropy (Astropy Collaboration et al.
1420 2013), emcee (Foreman-Mackey et al. 2013), corner

1424

APPENDIX

A. EXTENSION AND IHL FRACTION

1425 Table 5 summarize the fraction of light beyond 10 and
1426 20 kpc, assuming our fitted light profile. These are the
1427 data presented in Fig. 13.
1428

1421 (Foreman-Mackey 2016), astrometry.net (Lang et al.
1422 2010), LePHARE (Arnouts et al. 1999; Ilbert et al.
1423 2006)

1429 Table 6 summarize the f_{IHL} values with $r_{\text{cut}}=10$ and
1430 20 kpc, assuming our fitted light profile and the one-
1431 halo contribution from the MICECAT. These are the
1432 data presented in Fig. 15 and 16.

REFERENCES

- 1433 Abdalla, H., Adam, R., Aharonian, F., et al. 2020,
1434 MNRAS, 494, 5590, doi: [10.1093/mnras/staa999](https://doi.org/10.1093/mnras/staa999)
- 1435 Abdo, A. A., Ackermann, M., Ajello, M., et al. 2010, ApJ,
1436 723, 1082, doi: [10.1088/0004-637X/723/2/1082](https://doi.org/10.1088/0004-637X/723/2/1082)
- 1437 Abell, G. O. 1958, ApJS, 3, 211, doi: [10.1086/190036](https://doi.org/10.1086/190036)
- 1438 Abeyssekara, A. U., Archer, A., Benbow, W., et al. 2019,
1439 ApJ, 885, 150, doi: [10.3847/1538-4357/ab4817](https://doi.org/10.3847/1538-4357/ab4817)
- 1440 Abraham, R. G., & van Dokkum, P. G. 2014, PASP, 126,
1441 55, doi: [10.1086/674875](https://doi.org/10.1086/674875)
- 1442 Acciari, V. A., Ansoldi, S., Antonelli, L. A., et al. 2019,
1443 MNRAS, 486, 4233, doi: [10.1093/mnras/stz943](https://doi.org/10.1093/mnras/stz943)
- 1444 Ackermann, M., Ajello, M., Allafort, A., et al. 2012,
1445 Science, 338, 1190, doi: [10.1126/science.1227160](https://doi.org/10.1126/science.1227160)
- 1446 Ackermann, M., Ajello, M., Baldini, L., et al. 2018, ApJS,
1447 237, 32, doi: [10.3847/1538-4365/aacdf7](https://doi.org/10.3847/1538-4365/aacdf7)
- 1448 Aharonian, F., Akhperjanian, A. G., Bazer-Bachi, A. R.,
1449 et al. 2006, Nature, 440, 1018, doi: [10.1038/nature04680](https://doi.org/10.1038/nature04680)
- 1450 Aharonian, F., Akhperjanian, A. G., Barres de Almeida,
1451 U., et al. 2007, A&A, 475, L9,
1452 doi: [10.1051/0004-6361:20078462](https://doi.org/10.1051/0004-6361:20078462)
- 1453 Aihara, H., Allende Prieto, C., An, D., et al. 2011, ApJS,
1454 193, 29, doi: [10.1088/0067-0049/193/2/29](https://doi.org/10.1088/0067-0049/193/2/29)
- 1455 Arnouts, S., Cristiani, S., Moscardini, L., et al. 1999,
1456 MNRAS, 310, 540, doi: [10.1046/j.1365-8711.1999.02978.x](https://doi.org/10.1046/j.1365-8711.1999.02978.x)
- 1457 Astropy Collaboration, Robitaille, T. P., Tollerud, E. J.,
1458 et al. 2013, A&A, 558, A33,
1459 doi: [10.1051/0004-6361/201322068](https://doi.org/10.1051/0004-6361/201322068)
- 1460 Bernstein, R. A. 2007, ApJ, 666, 663, doi: [10.1086/519824](https://doi.org/10.1086/519824)
- 1461 Blanton, M. R., Bershadsky, M. A., Abolfathi, B., et al. 2017,
1462 AJ, 154, 28, doi: [10.3847/1538-3881/aa7567](https://doi.org/10.3847/1538-3881/aa7567)
- 1463 Bock, J., Sullivan, I., Arai, T., et al. 2013, ApJS, 207, 32,
1464 doi: [10.1088/0067-0049/207/2/32](https://doi.org/10.1088/0067-0049/207/2/32)
- 1465 Bruzual A., G., & Charlot, S. 1993, ApJ, 405, 538,
1466 doi: [10.1086/172385](https://doi.org/10.1086/172385)
- 1467 Bullock, J. S., & Johnston, K. V. 2005, ApJ, 635, 931,
1468 doi: [10.1086/497422](https://doi.org/10.1086/497422)
- 1469 Burke, C., Hilton, M., & Collins, C. 2015, MNRAS, 449,
1470 2353, doi: [10.1093/mnras/stv450](https://doi.org/10.1093/mnras/stv450)
- 1471 Carollo, D., Beers, T. C., Chiba, M., et al. 2010, ApJ, 712,
1472 692, doi: [10.1088/0004-637X/712/1/692](https://doi.org/10.1088/0004-637X/712/1/692)
- 1473 Carretero, J., Castander, F. J., Gaztañaga, E., Crocce, M.,
1474 & Fosalba, P. 2015, MNRAS, 447, 646,
1475 doi: [10.1093/mnras/stu2402](https://doi.org/10.1093/mnras/stu2402)
- 1476 Cavaliere, A., & Fusco-Femiano, R. 1978, A&A, 70, 677
- 1477 Chambers, K. C., Magnier, E. A., Metcalfe, N., et al. 2016,
1478 arXiv e-prints, arXiv:1612.05560.
1479 <https://arxiv.org/abs/1612.05560>
- 1480 Conroy, C., Wechsler, R. H., & Kravtsov, A. V. 2007, ApJ,
1481 668, 826, doi: [10.1086/521425](https://doi.org/10.1086/521425)
- 1482 Cooper, A. P., D'Souza, R., Kauffmann, G., et al. 2013,
1483 MNRAS, 434, 3348, doi: [10.1093/mnras/stt1245](https://doi.org/10.1093/mnras/stt1245)
- 1484 Cooper, A. P., Parry, O. H., Lowing, B., Cole, S., & Frenk,
1485 C. 2015, MNRAS, 454, 3185, doi: [10.1093/mnras/stv2057](https://doi.org/10.1093/mnras/stv2057)
- 1486 Cooper, A. P., Cole, S., Frenk, C. S., et al. 2010, MNRAS,
1487 406, 744, doi: [10.1111/j.1365-2966.2010.16740.x](https://doi.org/10.1111/j.1365-2966.2010.16740.x)
- 1488 Cooray, A. 2016, Royal Society Open Science, 3, 150555,
1489 doi: [10.1098/rsos.150555](https://doi.org/10.1098/rsos.150555)
- 1490 Cooray, A., & Sheth, R. 2002, PhR, 372, 1,
1491 doi: [10.1016/S0370-1573\(02\)00276-4](https://doi.org/10.1016/S0370-1573(02)00276-4)
- 1492 Cooray, A., Smidt, J., de Bernardis, F., et al. 2012, Nature,
1493 490, 514, doi: [10.1038/nature11474](https://doi.org/10.1038/nature11474)
- 1494 Courteau, S., Widrow, L. M., McDonald, M., et al. 2011,
1495 ApJ, 739, 20, doi: [10.1088/0004-637X/739/1/20](https://doi.org/10.1088/0004-637X/739/1/20)
- 1496 Crocce, M., Castander, F. J., Gaztañaga, E., Fosalba, P., &
1497 Carretero, J. 2015, MNRAS, 453, 1513,
1498 doi: [10.1093/mnras/stv1708](https://doi.org/10.1093/mnras/stv1708)
- 1499 Domínguez, A., Primack, J. R., Rosario, D. J., et al. 2011,
1500 MNRAS, 410, 2556,
1501 doi: [10.1111/j.1365-2966.2010.17631.x](https://doi.org/10.1111/j.1365-2966.2010.17631.x)

Table 5. Fraction of galaxy flux between 10/20 kpc and 100 kpc, assuming the galaxy light profile follows the stacking results in this work. These are the values shown in Fig. 13. The total row shows the weighted average of the five listed sub-samples.

Name	1.1 μm	1.1 μm	1.8 μm	1.8 μm
	10 kpc	20 kpc	10 kpc	20 kpc
high-M/low-z	$0.44^{+0.05}_{-0.05}$	$0.23^{+0.04}_{-0.04}$	$0.43^{+0.05}_{-0.04}$	$0.22^{+0.04}_{-0.04}$
high-M/med-z	$0.53^{+0.05}_{-0.04}$	$0.31^{+0.05}_{-0.04}$	$0.52^{+0.05}_{-0.04}$	$0.30^{+0.04}_{-0.04}$
high-M/high-z	$0.55^{+0.07}_{-0.05}$	$0.33^{+0.06}_{-0.05}$	$0.55^{+0.05}_{-0.04}$	$0.33^{+0.05}_{-0.04}$
low-M/low-z	$0.41^{+0.06}_{-0.05}$	$0.21^{+0.04}_{-0.04}$	$0.41^{+0.05}_{-0.05}$	$0.20^{+0.04}_{-0.04}$
low-M/med-z	$0.45^{+0.08}_{-0.06}$	$0.23^{+0.06}_{-0.05}$	$0.42^{+0.06}_{-0.05}$	$0.21^{+0.05}_{-0.04}$
total	$0.48^{+0.02}_{-0.03}$	$0.25^{+0.02}_{-0.02}$	$0.47^{+0.02}_{-0.02}$	$0.25^{+0.02}_{-0.02}$

Table 6. IHL fraction (Eq. 27) with $r_{\text{cut}} = 10/20$ kpc, assuming the galaxy light profile and the one-halo terms follow our stacking results and the MICECAT simulation, respectively. These are the values shown in Fig. 15 and 16. The total row shows the weighted average of the five listed sub-samples.

Name	1.1 μm	1.1 μm	1.8 μm	1.8 μm
	10 kpc	20 kpc	10 kpc	20 kpc
high-M/low-z	$0.44^{+0.09}_{-0.06}$	$0.23^{+0.06}_{-0.05}$	$0.40^{+0.06}_{-0.08}$	$0.21^{+0.04}_{-0.06}$
high-M/med-z	$0.51^{+0.12}_{-0.09}$	$0.30^{+0.09}_{-0.08}$	$0.44^{+0.08}_{-0.07}$	$0.26^{+0.06}_{-0.06}$
high-M/high-z	$0.31^{+0.10}_{-0.19}$	$0.19^{+0.07}_{-0.14}$	$0.24^{+0.06}_{-0.07}$	$0.15^{+0.04}_{-0.05}$
low-M/low-z	$0.41^{+0.10}_{-0.06}$	$0.21^{+0.07}_{-0.05}$	$0.41^{+0.09}_{-0.05}$	$0.21^{+0.06}_{-0.04}$
low-M/med-z	$0.44^{+0.23}_{-0.07}$	$0.23^{+0.14}_{-0.06}$	$0.29^{+0.09}_{-0.12}$	$0.15^{+0.05}_{-0.07}$
total	$0.43^{+0.03}_{-0.05}$	$0.23^{+0.03}_{-0.03}$	$0.36^{+0.03}_{-0.05}$	$0.19^{+0.02}_{-0.02}$

1502 Driver, S. P., Andrews, S. K., Davies, L. J., et al. 2016,
 1503 ApJ, 827, 108, doi: [10.3847/0004-637X/827/2/108](https://doi.org/10.3847/0004-637X/827/2/108)
 1504 D’Souza, R., Kauffman, G., Wang, J., & Vegetti, S. 2014,
 1505 MNRAS, 443, 1433, doi: [10.1093/mnras/stu1194](https://doi.org/10.1093/mnras/stu1194)
 1506 Elias, L. M., Sales, L. V., Creasey, P., et al. 2018, MNRAS,
 1507 479, 4004, doi: [10.1093/mnras/sty1718](https://doi.org/10.1093/mnras/sty1718)
 1508 Fernandez, E. R., Komatsu, E., Iliev, I. T., & Shapiro,
 1509 P. R. 2010, ApJ, 710, 1089,
 1510 doi: [10.1088/0004-637X/710/2/1089](https://doi.org/10.1088/0004-637X/710/2/1089)
 1511 Foreman-Mackey, D. 2016, The Journal of Open Source
 1512 Software, 1, 24, doi: [10.21105/joss.00024](https://doi.org/10.21105/joss.00024)
 1513 Foreman-Mackey, D., Hogg, D. W., Lang, D., & Goodman,
 1514 J. 2013, PASP, 125, 306, doi: [10.1086/670067](https://doi.org/10.1086/670067)
 1515 Fosalba, P., Crocce, M., Gaztañaga, E., & Castander, F. J.
 1516 2015a, MNRAS, 448, 2987, doi: [10.1093/mnras/stv138](https://doi.org/10.1093/mnras/stv138)
 1517 Fosalba, P., Gaztañaga, E., Castander, F. J., & Crocce, M.
 1518 2015b, MNRAS, 447, 1319, doi: [10.1093/mnras/stu2464](https://doi.org/10.1093/mnras/stu2464)

1519 Gaia Collaboration, Prusti, T., de Bruijne, J. H. J., et al.
 1520 2016, A&A, 595, A1, doi: [10.1051/0004-6361/201629272](https://doi.org/10.1051/0004-6361/201629272)
 1521 Gaia Collaboration, Brown, A. G. A., Vallenari, A., et al.
 1522 2018, A&A, 616, A1, doi: [10.1051/0004-6361/201833051](https://doi.org/10.1051/0004-6361/201833051)
 1523 Gelman, A., & Rubin, D. B. 1992, Statistical Science, 7,
 1524 457, doi: [10.1214/ss/1177011136](https://doi.org/10.1214/ss/1177011136)
 1525 Gonzalez, A. H., Zabludoff, A. I., & Zaritsky, D. 2005, ApJ,
 1526 618, 195, doi: [10.1086/425896](https://doi.org/10.1086/425896)
 1527 Gonzalez, A. H., Zaritsky, D., & Zabludoff, A. I. 2007, ApJ,
 1528 666, 147, doi: [10.1086/519729](https://doi.org/10.1086/519729)
 1529 Graham, A. W., Driver, S. P., Petrosian, V., et al. 2005,
 1530 AJ, 130, 1535, doi: [10.1086/444475](https://doi.org/10.1086/444475)
 1531 H. E. S. S. Collaboration, Abdalla, H., Abramowski, A.,
 1532 et al. 2017, A&A, 606, A59,
 1533 doi: [10.1051/0004-6361/201731200](https://doi.org/10.1051/0004-6361/201731200)
 1534 Hartlap, J., Simon, P., & Schneider, P. 2007, A&A, 464,
 1535 399, doi: [10.1051/0004-6361:20066170](https://doi.org/10.1051/0004-6361:20066170)

- 1536 Helgason, K., Ricotti, M., & Kashlinsky, A. 2012, *ApJ*, 752,
1537 113, doi: [10.1088/0004-637X/752/2/113](https://doi.org/10.1088/0004-637X/752/2/113)
- 1538 Hirata, C. M., & Choi, A. 2020, *PASP*, 132, 014501,
1539 doi: [10.1088/1538-3873/ab44f7](https://doi.org/10.1088/1538-3873/ab44f7)
- 1540 Hoffmann, K., Bel, J., Gaztañaga, E., et al. 2015, *MNRAS*,
1541 447, 1724, doi: [10.1093/mnras/stu2492](https://doi.org/10.1093/mnras/stu2492)
- 1542 Huang, S., Leauthaud, A., Greene, J. E., et al. 2018,
1543 *MNRAS*, 475, 3348, doi: [10.1093/mnras/stx3200](https://doi.org/10.1093/mnras/stx3200)
- 1544 Ilbert, O., Arnouts, S., McCracken, H. J., et al. 2006, *A&A*,
1545 457, 841, doi: [10.1051/0004-6361:20065138](https://doi.org/10.1051/0004-6361:20065138)
- 1546 Kashlinsky, A., Arendt, R. G., Ashby, M. L. N., et al. 2012,
1547 *ApJ*, 753, 63, doi: [10.1088/0004-637X/753/1/63](https://doi.org/10.1088/0004-637X/753/1/63)
- 1548 Kashlinsky, A., Arendt, R. G., Mather, J., & Moseley,
1549 S. H. 2005, *Nature*, 438, 45, doi: [10.1038/nature04143](https://doi.org/10.1038/nature04143)
- 1550 Kawara, K., Matsuoka, Y., Sano, K., et al. 2017, *PASJ*, 69,
1551 31, doi: [10.1093/pasj/psx003](https://doi.org/10.1093/pasj/psx003)
- 1552 Keenan, R. C., Barger, A. J., Cowie, L. L., & Wang, W. H.
1553 2010, *ApJ*, 723, 40, doi: [10.1088/0004-637X/723/1/40](https://doi.org/10.1088/0004-637X/723/1/40)
- 1554 Kim, M. G., Matsumoto, T., Lee, H. M., et al. 2019, *PASJ*,
1555 71, 82, doi: [10.1093/pasj/psz063](https://doi.org/10.1093/pasj/psz063)
- 1556 Korngut, P. M., Renbarger, T., Arai, T., et al. 2013, *ApJS*,
1557 207, 34, doi: [10.1088/0067-0049/207/2/34](https://doi.org/10.1088/0067-0049/207/2/34)
- 1558 Koushan, S., Driver, S. P., Bellstedt, S., et al. 2021, *arXiv*
1559 e-prints, arXiv:2102.12323.
1560 <https://arxiv.org/abs/2102.12323>
- 1561 Lang, D., Hogg, D. W., Mierle, K., Blanton, M., & Roweis,
1562 S. 2010, *AJ*, 139, 1782,
1563 doi: [10.1088/0004-6256/139/5/1782](https://doi.org/10.1088/0004-6256/139/5/1782)
- 1564 Lauer, T. R., Postman, M., Weaver, H. A., et al. 2020,
1565 *arXiv e-prints*, arXiv:2011.03052.
1566 <https://arxiv.org/abs/2011.03052>
- 1567 Levenson, L. R., Wright, E. L., & Johnson, B. D. 2007,
1568 *ApJ*, 666, 34, doi: [10.1086/520112](https://doi.org/10.1086/520112)
- 1569 Lin, Y.-T., & Mohr, J. J. 2004, *ApJ*, 617, 879,
1570 doi: [10.1086/425412](https://doi.org/10.1086/425412)
- 1571 Lucy, L. B. 1974, *AJ*, 79, 745, doi: [10.1086/111605](https://doi.org/10.1086/111605)
- 1572 MAGIC Collaboration, Albert, J., Aliu, E., et al. 2008,
1573 *Science*, 320, 1752, doi: [10.1126/science.1157087](https://doi.org/10.1126/science.1157087)
- 1574 Martínez-Delgado, D., Gabany, R. J., Crawford, K., et al.
1575 2010, *AJ*, 140, 962, doi: [10.1088/0004-6256/140/4/962](https://doi.org/10.1088/0004-6256/140/4/962)
- 1576 Matsumoto, T., Kim, M. G., Pyo, J., & Tsumura, K. 2015,
1577 *ApJ*, 807, 57, doi: [10.1088/0004-637X/807/1/57](https://doi.org/10.1088/0004-637X/807/1/57)
- 1578 Matsumoto, T., & Tsumura, K. 2019, *PASJ*, 71, 88,
1579 doi: [10.1093/pasj/psz070](https://doi.org/10.1093/pasj/psz070)
- 1580 Matsumoto, T., Tsumura, K., Matsuoka, Y., & Pyo, J.
1581 2018, *AJ*, 156, 86, doi: [10.3847/1538-3881/aad0f0](https://doi.org/10.3847/1538-3881/aad0f0)
- 1582 Matsumoto, T., Seo, H. J., Jeong, W. S., et al. 2011, *ApJ*,
1583 742, 124, doi: [10.1088/0004-637X/742/2/124](https://doi.org/10.1088/0004-637X/742/2/124)
- 1584 Matsuura, S., Arai, T., Bock, J. J., et al. 2017, *ApJ*, 839, 7,
1585 doi: [10.3847/1538-4357/aa6843](https://doi.org/10.3847/1538-4357/aa6843)
- 1586 Mitchell-Wynne, K., Cooray, A., Gong, Y., et al. 2015,
1587 *Nature Communications*, 6, 7945,
1588 doi: [10.1038/ncomms8945](https://doi.org/10.1038/ncomms8945)
- 1589 Muzzin, A., Marchesini, D., Stefanon, M., et al. 2013, *ApJ*,
1590 777, 18, doi: [10.1088/0004-637X/777/1/18](https://doi.org/10.1088/0004-637X/777/1/18)
- 1591 Petrosian, V. 1976, *ApJL*, 210, L53, doi: [10.1086/182301](https://doi.org/10.1086/182301)
- 1592 Planck Collaboration, Ade, P. A. R., Aghanim, N., et al.
1593 2016, *A&A*, 594, A13, doi: [10.1051/0004-6361/201525830](https://doi.org/10.1051/0004-6361/201525830)
- 1594 Purcell, C. W., Bullock, J. S., & Zentner, A. R. 2007, *ApJ*,
1595 666, 20, doi: [10.1086/519787](https://doi.org/10.1086/519787)
- 1596 —. 2008, *MNRAS*, 391, 550,
1597 doi: [10.1111/j.1365-2966.2008.13938.x](https://doi.org/10.1111/j.1365-2966.2008.13938.x)
- 1598 Richardson, W. H. 1972, *Journal of the Optical Society of*
1599 *America* (1917-1983), 62, 55
- 1600 Rodriguez-Gomez, V., Pillepich, A., Sales, L. V., et al.
1601 2016, *MNRAS*, 458, 2371, doi: [10.1093/mnras/stw456](https://doi.org/10.1093/mnras/stw456)
- 1602 Rowan-Robinson, M., Gonzalez-Solares, E., Vaccari, M., &
1603 Marchetti, L. 2013, *MNRAS*, 428, 1958,
1604 doi: [10.1093/mnras/sts163](https://doi.org/10.1093/mnras/sts163)
- 1605 Rowan-Robinson, M., Babbedge, T., Oliver, S., et al. 2008,
1606 *MNRAS*, 386, 697, doi: [10.1111/j.1365-2966.2008.13109.x](https://doi.org/10.1111/j.1365-2966.2008.13109.x)
- 1607 Rudick, C. S., Mihos, J. C., Frey, L. H., & McBride, C. K.
1608 2009, *ApJ*, 699, 1518,
1609 doi: [10.1088/0004-637X/699/2/1518](https://doi.org/10.1088/0004-637X/699/2/1518)
- 1610 Rudy, R. J., Woodward, C. E., Hodge, T., Fairfield, S. W.,
1611 & Harker, D. E. 1997, *Nature*, 387, 159,
1612 doi: [10.1038/387159a0](https://doi.org/10.1038/387159a0)
- 1613 Saldana-Lopez, A., Domínguez, A., Pérez-González, P. G.,
1614 et al. 2020, *arXiv e-prints*, arXiv:2012.03035.
1615 <https://arxiv.org/abs/2012.03035>
- 1616 Sano, K., Kawara, K., Matsuura, S., et al. 2015, *ApJ*, 811,
1617 77, doi: [10.1088/0004-637X/811/2/77](https://doi.org/10.1088/0004-637X/811/2/77)
- 1618 Sano, K., Matsuura, S., Yomo, K., & Takahashi, A. 2020,
1619 *ApJ*, 901, 112, doi: [10.3847/1538-4357/abad3d](https://doi.org/10.3847/1538-4357/abad3d)
- 1620 Seo, H. J., Lee, H. M., Matsumoto, T., et al. 2015, *ApJ*,
1621 807, 140, doi: [10.1088/0004-637X/807/2/140](https://doi.org/10.1088/0004-637X/807/2/140)
- 1622 Skrutskie, M. F., Cutri, R. M., Stiening, R., et al. 2006, *AJ*,
1623 131, 1163, doi: [10.1086/498708](https://doi.org/10.1086/498708)
- 1624 Symons, T., Zemcov, M., Bock, J., et al. 2021, *ApJS*, 252,
1625 24, doi: [10.3847/1538-4365/abcaa5](https://doi.org/10.3847/1538-4365/abcaa5)
- 1626 Tal, T., & van Dokkum, P. G. 2011, *ApJ*, 731, 89,
1627 doi: [10.1088/0004-637X/731/2/89](https://doi.org/10.1088/0004-637X/731/2/89)
- 1628 Tal, T., van Dokkum, P. G., Nelan, J., & Bezanson, R.
1629 2009, *AJ*, 138, 1417, doi: [10.1088/0004-6256/138/5/1417](https://doi.org/10.1088/0004-6256/138/5/1417)
- 1630 Thompson, R. I., Eisenstein, D., Fan, X., Rieke, M., &
1631 Kennicutt, R. C. 2007, *ApJ*, 666, 658,
1632 doi: [10.1086/520634](https://doi.org/10.1086/520634)
- 1633 Tsumura, K., Matsumoto, T., Matsuura, S., Sakon, I., &
1634 Wada, T. 2013a, *PASJ*, 65, 121,
1635 doi: [10.1093/pasj/65.6.121](https://doi.org/10.1093/pasj/65.6.121)

- 1636 Tsumura, K., Arai, T., Battle, J., et al. 2013b, *ApJS*, 207,
1637 33, doi: [10.1088/0067-0049/207/2/33](https://doi.org/10.1088/0067-0049/207/2/33)
- 1638 van Dokkum, P. G., Abraham, R., & Merritt, A. 2014,
1639 *ApJL*, 782, L24, doi: [10.1088/2041-8205/782/2/L24](https://doi.org/10.1088/2041-8205/782/2/L24)
- 1640 Wang, W., Han, J., Sonnenfeld, A., et al. 2019, *MNRAS*,
1641 487, 1580, doi: [10.1093/mnras/stz1339](https://doi.org/10.1093/mnras/stz1339)
- 1642 Wen, Z. L., Han, J. L., & Liu, F. S. 2012, *ApJS*, 199, 34,
1643 doi: [10.1088/0067-0049/199/2/34](https://doi.org/10.1088/0067-0049/199/2/34)
- 1644 Zemcov, M., Immel, P., Nguyen, C., et al. 2017, *Nature*
1645 *Communications*, 8, 15003, doi: [10.1038/ncomms15003](https://doi.org/10.1038/ncomms15003)
- 1646 Zemcov, M., Arai, T., Battle, J., et al. 2013, *ApJS*, 207, 31,
1647 doi: [10.1088/0067-0049/207/2/31](https://doi.org/10.1088/0067-0049/207/2/31)
- 1648 Zemcov, M., Smidt, J., Arai, T., et al. 2014, *Science*, 346,
1649 732, doi: [10.1126/science.1258168](https://doi.org/10.1126/science.1258168)
- 1650 Zhang, Y., Yanny, B., Palmese, A., et al. 2019, *ApJ*, 874,
1651 165, doi: [10.3847/1538-4357/ab0dfd](https://doi.org/10.3847/1538-4357/ab0dfd)
- 1652 Zibetti, S., White, S. D. M., Schneider, D. P., &
1653 Brinkmann, J. 2005, *MNRAS*, 358, 949,
1654 doi: [10.1111/j.1365-2966.2005.08817.x](https://doi.org/10.1111/j.1365-2966.2005.08817.x)
- 1655 Zu, Y., & Mandelbaum, R. 2015, *MNRAS*, 454, 1161,
1656 doi: [10.1093/mnras/stv2062](https://doi.org/10.1093/mnras/stv2062)